# AMERICAN UNIVERSITY OF BEIRUT

# ULTRASONIC WAVES TIME SERIES ANALYSIS FOR DAMAGE DETECTION AND ASSESSMENT IN COMPOSITE AND METALLIC STRUCTURES

by
# MOHAMMAD ALI HASSAN FAKIH

A thesis
submitted in partial fulfillment of the requirements
for the degree of Master of Engineering
to the Department of Mechanical Engineering
of the Faculty of Engineering and Architecture
at the American University of Beirut

Beirut, Lebanon
September 2016

AMERICAN UNIVERSITY OF BEIRUT

ULTRASONIC WAVES TIME SERIES ANALYSIS FOR
DAMAGE DETECTION AND ASSESSMENT IN COMPOSITE
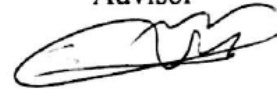AND METALLIC STRUCTURES

by
MOHAMMAD ALI HASSAN FAKIH

Approved by:

_____
Dr. Samir Mustapha, Assistant Professor                    Advisor
Department of Mechanical Engineering
Faculty of Engineering and Architecture
American University of Beirut

_____
Dr. Ramsey Hamade, Professor                    Member of Committee
Department of Mechanical Engineering
Faculty of Engineering and Architecture
American University of Beirut

_____
Dr. Georges Ayoub, Assistant Professor          Member of Committee
Industrial and Manufacturing Systems
Engineering Department
University of Michigan Dearborn

Date of thesis defense: September 9, 2016

# AMERICAN UNIVERSITY OF BEIRUT

# THESIS, DISSERTATION, PROJECT RELEASE FORM

Student Name: _____
                          Last                          First                          Middle

◯ Master's Thesis          ◯ Master's Project          ◯ Doctoral Dissertation

☐      I authorize the American University of Beirut to: (a) reproduce hard or electronic copies of my thesis, dissertation, or project; (b) include such copies in the archives and digital repositories of the University; and (c) make freely available such copies to third parties for research or educational purposes.

☐      I authorize the American University of Beirut, **three years after the date of submitting my thesis, dissertation, or project,** to: (a) reproduce hard or electronic copies of it; (b) include such copies in the archives and digital repositories of the University; and (c) make freely available such copies to third parties for research or educational purposes.

_____

Signature                                                        Date

# ACKNOWLEDGMENTS

The most special thanks and love are for those who are always there for me, those who have borne and will always bear all the difficulties to stand by my side, those whom no matter how much I thank, I will never pay them back, for my supporting friends, for my tender family, for my precious parents, for my adorable wife, and for my lovely son.

# AN ABSTRACT OF THE THESIS OF

Mohammad Ali Hassan Fakih     for     Master of Engineering
                                                 Major: Mechanical Engineering

Title: Ultrasonic Waves Time Series Analysis for Damage Detection and Assessment in Composite and Metallic Structures

Ultrasonic guided waves (Lamb waves) are widely used for damage detection and structural health monitoring in mechanical, aerospace and civil structures. In this work, various signal processing and feature extraction techniques are applied on Lamb waves for damage assessment in both metallic and composite structures. Waves are excited at different frequencies and the fundamental symmetric (S0) mode was chosen to monitor different types of damage including flaws in welded metal structures, and barely visible indentation damage (BVID) in composite structures resulting from low speed impacts.

The attenuation of the signal amplitude was first used as the feature to define a damage index (DI) which was used later to identify flaws in friction-stir-welded AZ31B magnesium alloy plates. Four plates of various weld qualities and a non-welded plate were used for investigation, where the DI was proposed as a comparison between the responses in the welded plates and the non-welded one. The S0 mode was separated using the improved complete ensemble empirical mode decomposition with adaptive noise "improved CEEMDAN" technique. On the other hand, computed tomography (CT) scanning was used as a non-destructive testing (NDT) to determine the actual weld qualities, and the method was further verified using finite element analysis (FEA). The proposed approach was highly sensitive to internal flaws within the weld and further had a great potential to classify the quality of weld in the various tested specimens.

In addition, the S0 mode was used to assess barely visible indentation damage (BVID) in a carbon fiber reinforced epoxy (CF/EP) composite structure using symbolic time series analysis (STSA). STSA transforms a time series into a symbol sequence according to a pre-constructed symbol space using a set number of partitions. The symbolization technique allows keeping only the probability vectors of symbols' occurrence as a feature. This reduces data and computational time significantly. A quasi-static loading was gradually applied on a specimen, and the resulting dent size varied between 0.2 mm to 2.7 mm. Waves were captured from a sensor network of 16 piezoelectric elements mounted on the surface of the tested panel. The number of partitions for creating the symbol space was selected based on the maximum Shannon's entropy approach. After that, a DI was established depending on the ratio of the norms of probability vectors before and after damage, and an imaging algorithm was

implemented to localize damages. The approach showed high sensitivity to a very small change of 0.2 mm on the surface, the locations of small impacts were precisely predicted, and the ability to detect progressive damage was demonstrated.

# CONTENTS

# ILLUSTRATIONS

# TABLES

# CHAPTER I

# INTRODUCTION

It is very well known that an invisible or a buried damage in the structure may develop into bigger cracks and consequently endanger the reliability of the whole structure. This damage, if not detected, may lead to structure failure [1] which is sometimes disastrous. Structural health monitoring (SHM) is the act of monitoring a structure periodically or continuously for assessing the technical condition and detecting any damage that may appear in any part of the structure to prevent failure. There are four stages of identifying the condition of a structure: detection, localization, identification and prediction [2]. Some also propose an additional stage called classification between the localization and identification [3].

Over the years many non-destructive testing (NDT) methods have been developed and commonly used to control the quality of structural components after manufacturing, and to check structural integrity during the life of service [4]. They can be local or global NDTs. Locals include ultrasonic, eddy current, radiographic, thermographic, dye penetration, and magnetic dust methods [1]. Local NDTs necessitate the repetition of the tests on all the areas that are exposed to damage availability; they are time-consuming, labor intensive, require experienced personnel, costly, and most importantly can't reach all structure parts and sometimes need to disrupt the structure functionality while inspected [1]. For this reason, researches are focused on global NDTs including vibration methods and methods using ultrasonic guided waves (Lamb waves). Global NDTs permit periodic observation of monitored structures while they

are still in normal operation. They do not need any special preparation except the first implementation of sensors, and do not require experienced personnel. However, an important drawback of these methods is their sensitivity to noise and signal distortion.

Lamb waves are ultrasonic elastic waves which have the ability of long travels through structures even in materials possessing high weakening ratio such as CF/EP composites. Their ability to propagate in complex structures and in both metallic and non-metallic materials, has drawn the attention of many researchers and manufacturers. Different Lamb modes offer the possibility of discovering surface and internal damage by examining the whole laminate thickness [5]. Over the last decades, Lamb waves have been involved in tens of research topics for non-destructive testing (NDT) and structural health monitoring (SHM) applications. They have proven proficiency, having been widely used to develop various damage identification algorithms for assessing fatigue cracking, delamination, fiber breakage, de-bonding, holes, cracks/notches and corrosion in composite and metallic plate-like structures [6-20].

The current research focuses on detection, localization, and identification of damage or defect by means of Lamb waves time series analysis. Two applications will be presented in the following sections proving the potential of Lamb waves in determining weld quality in friction-stir-welded metallic structures, and in the detection and assessment of barely visible indentation damages (BVID) in composites sandwich structures. Each of the applications has its own different data analysis methods that were investigated and used.

# CHAPTER II

# DAMAGE DETECTION AND ASSESSMENT IN FRICTION STIR WELDING

## A.  Introduction

Friction stir welding (FSW) is an important novel welding process used in industry of cars, boats, airplanes, phones, and many others. It has made a large impact on the welding community for the past two decades and attracted the attention of many research engineers, academics and industry people. As other welding processes, many variables have a direct impact on the quality of obtained welds, where the welding parameters should be optimized for every specific application. However, not all welding defects are detectable by the naked-eye, and therefore weld inspection by man is actually unfeasible. After parameters' optimization, monitoring the qualities of welds during fabrication is essential to detect and correct any variation in the weld conditions or to recalibrate when needed. Furthermore, structural health monitoring (SHM) of metallic structures containing FSW is also important as a preventive measure to avoid their failure.

FSW is a novel environment-friendly solid state welding process [21]. It was invented and validated by W. Thomas and his colleagues at The Welding Institute (TWI) in UK in 1991 [22, 23], and has been proven to be an effective joining method which takes place at a temperature lower than the welded metal's melting point [24, 25]. Since the metal is exposed to less heat, it does not undergo total melting which leads to many advantages [21], some of which are summarized in Table 1 [21, 26].

**Table 1: Advantages of friction stir welding over traditional welding processes [21, 26].**

| FSW Advantages | |
|---|---|
| Metallurgical:<br>• Good steadiness in dimensions<br>• Potential of being repeatable<br>• No need for filling materials<br>• Exceptional mechanical properties in weld region<br>• Avoid other weld imperfections as porosity & solidification cracking | Environmental:<br>• No grinding wastes<br>• No harmful emissions<br>• Minimum need for surface cleaning |

FSW has found its way into high production since 1996, however this does not eliminate some of the disadvantages of the process. Disadvantages include leaving a hole behind when the tool is withdrawn, requiring a large down force, and being less flexible than manual and arc welding processes [27].

The FSW is performed using a non-consumable rotating cylindrical tool whose pin is inserted into the adjacent edges of the sheets/plates to be joined, and is traversed along the line of joint (Figure 1). The pin is slightly shorter than the required weld depth, and the shoulder is pushed down on the plates' surfaces causing a high frictional force while rotating. In this way, the tool provides the heating to the workpiece, and also ensures the flow of the material to produce the joint.

Hamade et al. [28-31] at the American University of Beirut (AUB) have been heavily involved in the area of FSW. Numerical simulation of the FSW process was developed for twin roll cast roll AZ31B. The authors have worked on the improvement of the microstructure of friction stir welded aluminum alloy joint by using several cooling techniques, based on temperature controlled backing plate and another technique via cryogenic $CO_2$ direct nozzle. In addition, a numerical FEM thermo-

4

mechanical based model have been used for optimizing the process parameters, including active in-process cooling. Moreover, they have carried numerical and experimental work on the application of FSW in bimetallic structures. The authors investigated the distribution of aluminum and magnesium within the joints they have produced using X-ray spectroscopy, as well as identifying the intermetallic compound using X-ray diffraction (XRD) [32, 33].
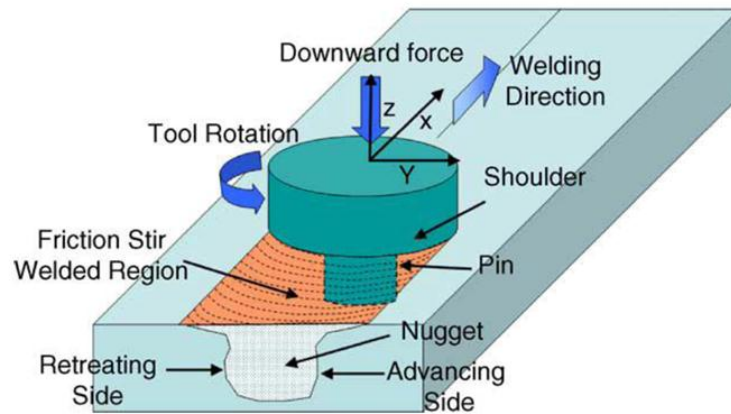


**Figure 1: Schematic of the friction stir welding process [34].**

Figure 2 shows a schematic of FSW in-plate zones [21, 35]. Different factors like process parameters, geometry of the tool, working piece temperature and its thermal conductivity all affect the nugget's shape [34] (Figure 3). The nugget is usually slightly larger than the pin diameter [21]. Defects, that FSW is exposed to, differ from those of fusion welding. The wrong selection of process parameters may cause one or more of defects such as worm hole, scalloping, ribbon flash, surface lack of fill, nugget collapse, and surface galling (see Figure 4) [36]. Therefore, FSW may not be defect free

and therefore a quality inspection method is a necessity to ensure adequate performance during service.
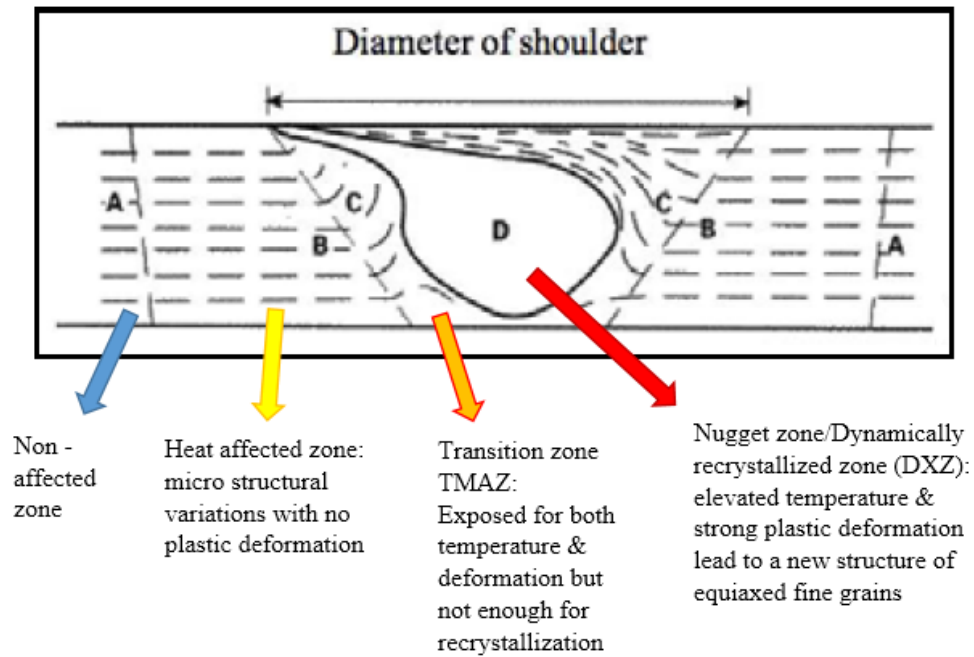


**Figure 2: Friction Stir Welding in-plate zones [21, 35].**
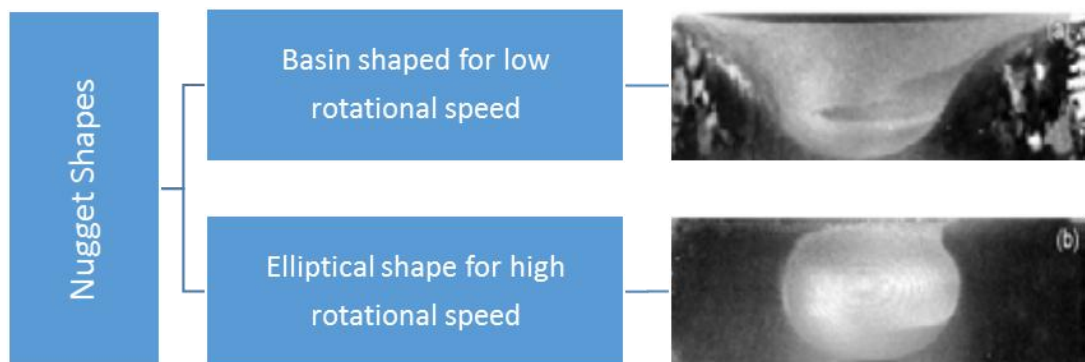


**Figure 3: Nugget zone's two common shapes [37].**
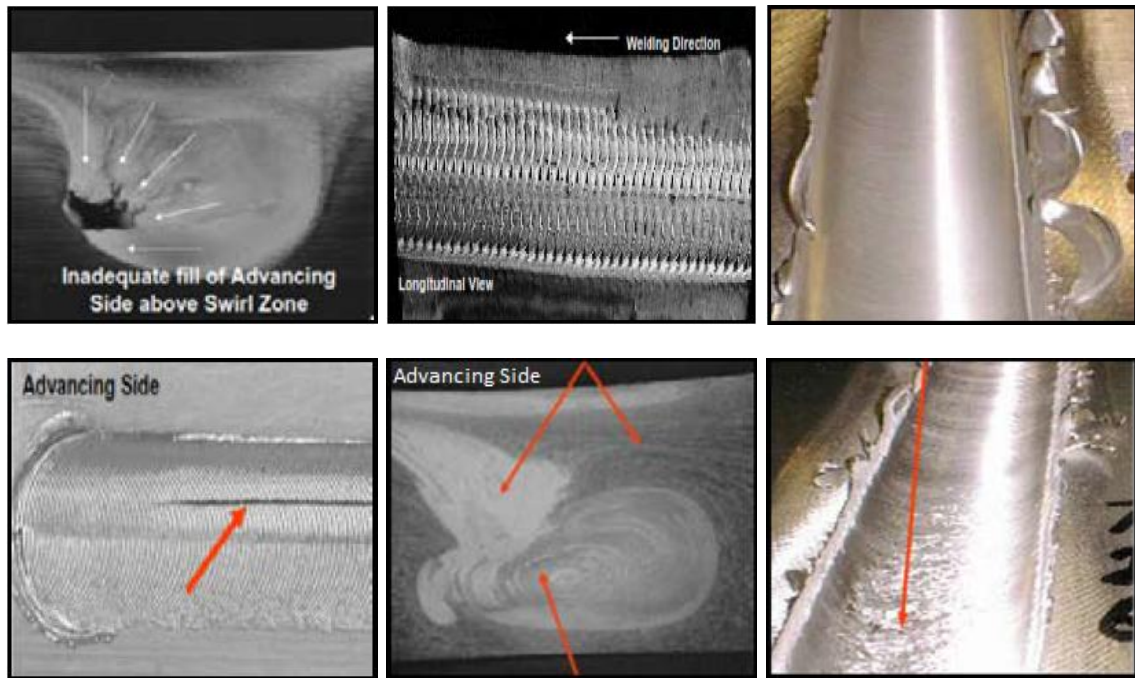
**Figure 4: FSW defects, from the left to the right, 1st then 2nd row: worm hole, scalloping, ribbon flash, surface lack of fill, nugget collapse, and surface galling [36].**

Several non-destructive testing methods are available for quality control of welds including visual inspection, acoustic emission, Eddy current, and ultrasonics. As visual inspection can't detect the possibly buried defects of FSW, the other techniques are capable of inspecting only a specific region of a structure; in addition, these techniques can be very time-consuming and labor-intensive, or even may not be feasible in complicated structures.

The use of ultrasonics for weld inspection is not a recent technology. Many researches have been done investigating the abilities of various ultrasonic testing methods for assessing different kinds of welds. In 1986, Burch et al. [38] have used pulse-echo multi-angle ultrasound scanning to detect and classify various types of hidden weld defects in ferritic steels. They established physical models of ultrasound interaction with such kinds of defect. After that, three features were chosen to develop

7

the automated classifier. In 1992, Karim et al. [39] have studied the scattering of an elastic wave in a plate containing inclusions and/or cracks by both numerical and analytical means. The effects of different kinds of inclusions and crack shapes and sizes were studied. In the case of two welded aluminum plates, they found that the weld has decreased the magnitude of the displacement spectra in the horizontal direction more than the direction normal to the surface. In the same year, Alleyne et al. [40] argued the choice of the proper mode and frequency range of Lamb waves for diverse examination desires. They reviewed ways of excitation, measurement, and processing. They also had shown that flaws can be efficiently recognized from the variations in the form of the waves when working below the second anti-symmetric mode ($a_1$) cut-off frequency. In 1999, Dixon et al. [41] proposed a combined laser-EMAT system, where EMAT stands for electromagnetic acoustic transducer, for ultrasonic weld examination. They suggested that the system can be suitable for a quick pre-screening inspection to tell the presence of defects in the weld because it is not sensitive to all types and sizes of defects. In 2003, Cawley et al. [42] have discussed the difficulties of guided wave testing and the ways to solve those difficulties in order to make them progress from research to practical and real commercial applications. Examples about pipes, railroads and other applications were provided. Three years later, Kažys et al. [43] studied the interaction between guided waves and welds or other irregularities in liquid-loaded steel plates as tank floors. They found by experiments and numerical simulations that a defect or a weld reflects acoustic energy into the liquid which can be caught to reveal the location of the flaw. On the other hand, Arone et al. [44] made use of both non-contact pulsed laser and contact angle-beam actuators to excite ultrasonic waves in aluminum welded joints. The two kinds of waves were received by an air-coupled

sensor and used to locate and characterize the defects respectively. Later on, Lu et al. [45] proved that Lamb waves induced and sensed by means of PZT wafers have the potential of spotting and localizing welds, cracks, and cracks containing different kinds of impurities in steel plates. The authors compared the peak-to-peak amplitudes of the incident and damage-reflected waves to identify cracks. They have used several signal processing and pattern recognition techniques in addition to numerical simulation for validation. Recently, different signal processing and pattern recognition techniques applied on ultrasonic testing, were studied and proposed for the assessment of the quality of resistance spot welding [46, 47].

Concerning FSW, Santos et al. [48] have investigated the ability of Lamb waves to assess FSW in aluminum plates in comparison to x-ray and C-scan inspection methods. They used a pitch-catch setup while doing a mechanical scanning along the line of the weld in a water medium. They found that their technique is more efficient in qualitative classification of linear FSW in aluminum plates than x-ray and C-scan in terms of simplicity, time, and expenses. On the other hand, the authors found that this technique still gives uncertain discrimination for very small weld flaws.

In a recent study, Tabatabaeipour et al. [49] have used also an immersion setup and a pitch/catch technique, to capture the non-linear features that occur in the reflected signals because of FSW kissing bond defects. The authors have used Fermat design transducers to focus and receive ultrasonic shear waves in aluminum welded plates. The signals were then analyzed by means of pulse inversion, and the results were validated numerically and experimentally. In another work [50], and in an immersion setup too, the same author used an angle-beam technique for ultrasonic inspection of FSW aluminum butt-joints. After scanning the whole weld in the cross sectional and

longitudinal directions, they could detect and qualitatively identify the kind and severity of root flaws by looking at the backscattered energy from the bottom of the weld.

To look from a practical point of view, structures that should undergo NDT as airplanes, cars, even boats, or other metallic structures, can't be totally immersed in water for each testing. The more practical solution is to place an actuating transducer somewhere on the structure and sense the response by another sensing transducer placed somewhere else [39].

This study will aim at the development of a method based on ultrasonic guided waves as a tool to inspect welds, with particular focus on friction stir welds. A qualification approach based on mode separation using improved CEEMDAN is proposed to assess the quality of FSW in magnesium alloy plates using ultrasonic guided Lamb waves. Different weld qualities were determined by varying the weld parameters. Lamb waves were actuated and received by means of piezoelectric ceramics (PZTs). The complex waves were separated into multiple modes using improved CEEMDAN, and the damage index (DI) of each weld was calculated according to the amplitude variation of the wave transmitted through the weld in comparison to the non-welded plate. The results were compared to CT-scans and their corresponding finite element analysis for validations. Finally, an equation was suggested between the damage volume and the measured DI from the working frequency that gave the highest precision, and a case study was addressed.

## B. Experimental Setup

An experiment set-up was established as illustrated in Figure 5. PZT wafers were used to actuate and receive wave signals across the weld. 4 ultrasonic wave signals of 5 cycles each and of frequencies 200, 300, 400, and 500 KHz were generated at a sampling rate of 20MSa/s using Matlab. The signals were saved to an arbitrary waveform generator. The arbitrary waveform generator was used to feed the signals into a power amplifier with a peak to peak amplitude of 5 volts. The amplifier in turn amplifies the signals to a peak to peak amplitude of 60V before they are fed one by one into the actuator PZT. A high rate acquisition oscilloscope, containing a signal conditioner, was employed to capture the wave signals of both the input fed into the actuator PZT and the output received by the sensor PZT.
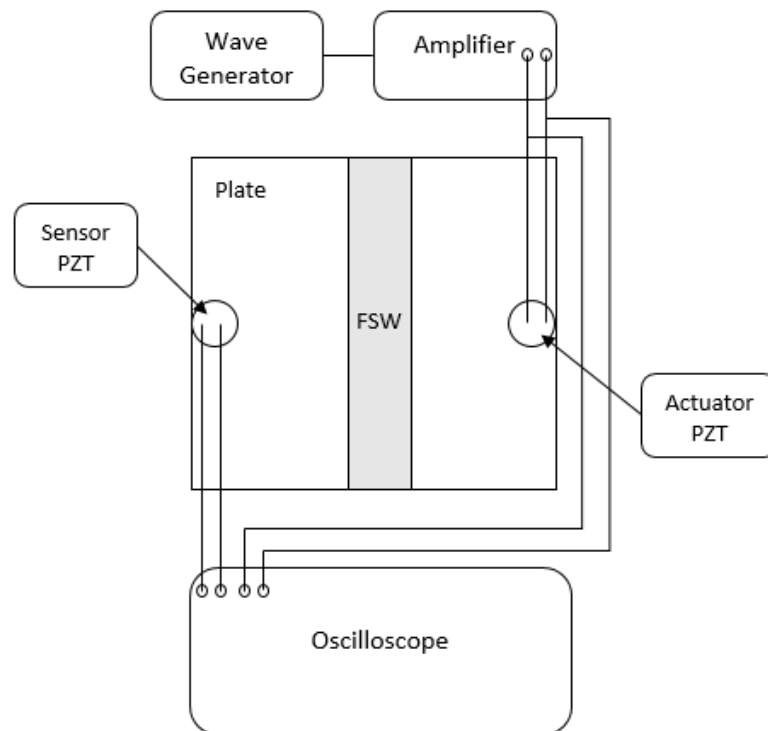


**Figure 5: Schematic of the experimental setup.**

Four plates of various weld qualities were produced by varying one of the FSW process parameters, and a fifth non-welded plate was used for comparison.

The tested plates material was AZ31B magnesium alloy. They had approximately the same dimensions of 100 x 94 x 3 mm with some minor variations due to deformations occurring during the FSW process. All welds were accomplished with a turning speed of 1200 RPM and an advancing speed of 150 mm/hr. Table 2 shows the variable parameter of the FSW process while producing our testing specimens which is the pin insertion. The plates numbering is according to the order they were provided, with no significance to the weld quality, and the non-welded plate was named as Plate 0. Figure 6 shows all the plates with their corresponding numbers.

**Table 2: FSW variable parameter among the specimens.**

| Plate number | Pin Insertion (mm) |
| --- | --- |
| 0 | No weld |
| 1 | 2.75 |
| 2 | 2.725 |
| 3 | 2.85 |
| 4 | 2.87 |
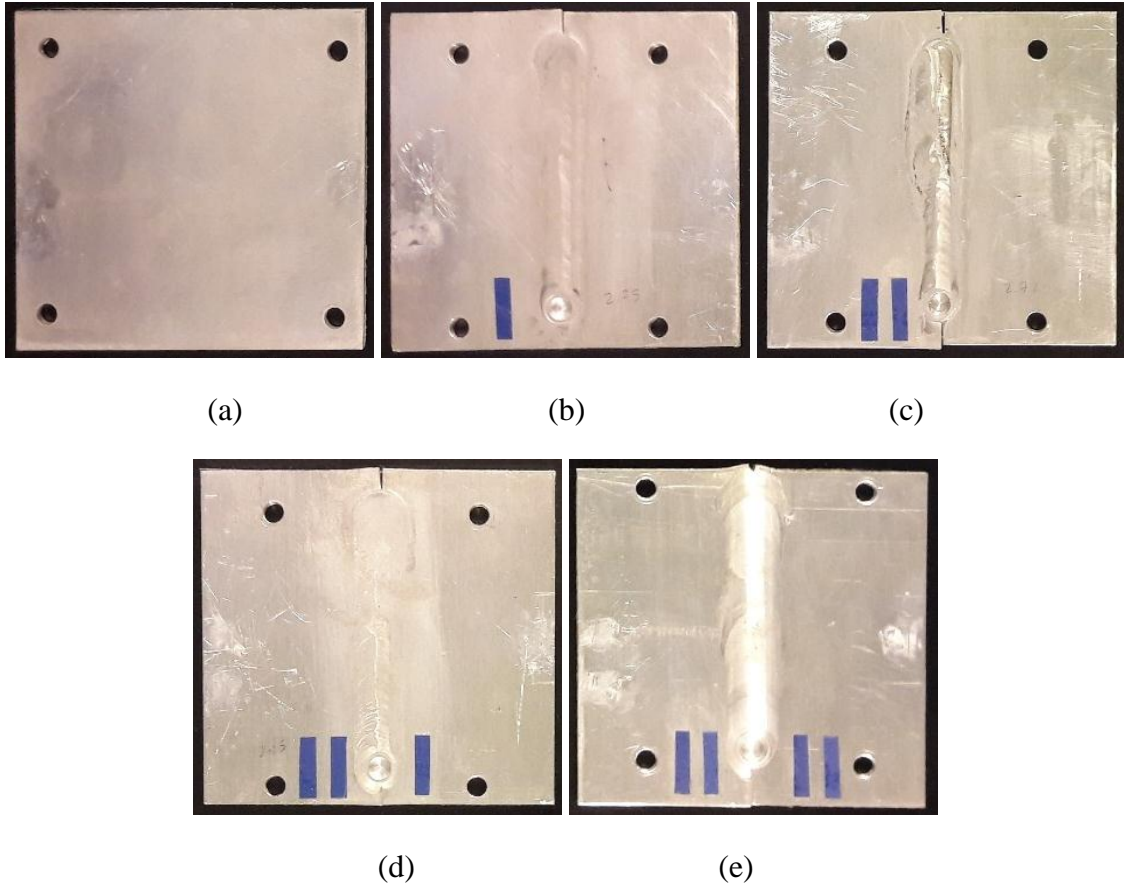
**Figure 6: The five tested plates named from (a) to (e): Plate0 to Plate4.**

To have similar boundary conditions for all the measurements and to reduce noise effects. The plates were fixed by double sided tapes on plexi-glass plates which were in turn fixed to a damping table. Figure 7 shows a schematic and a real photo of the plates' setup.
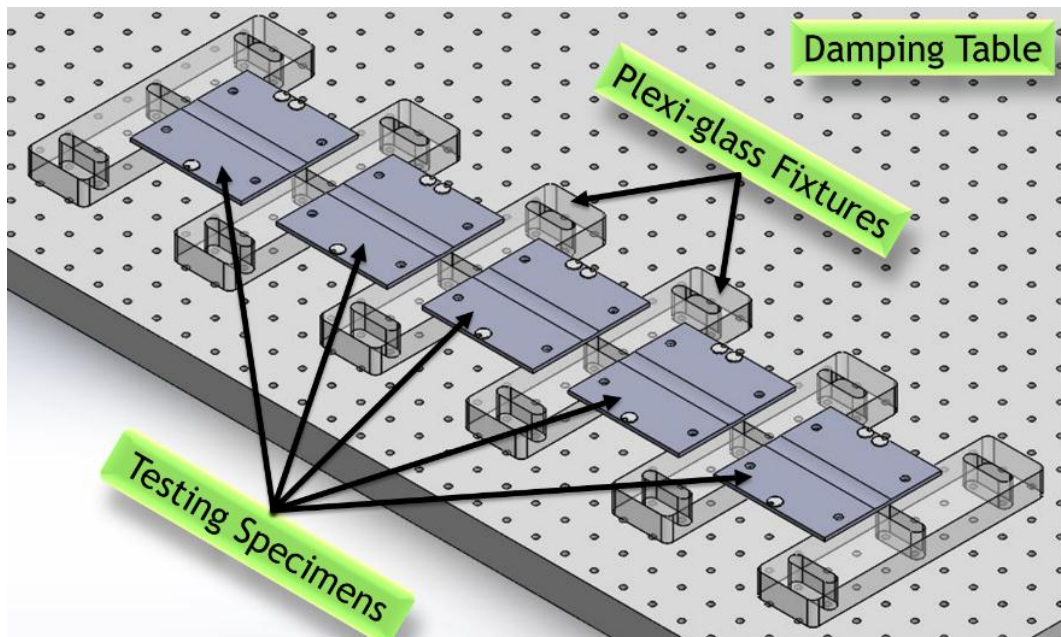
(a)
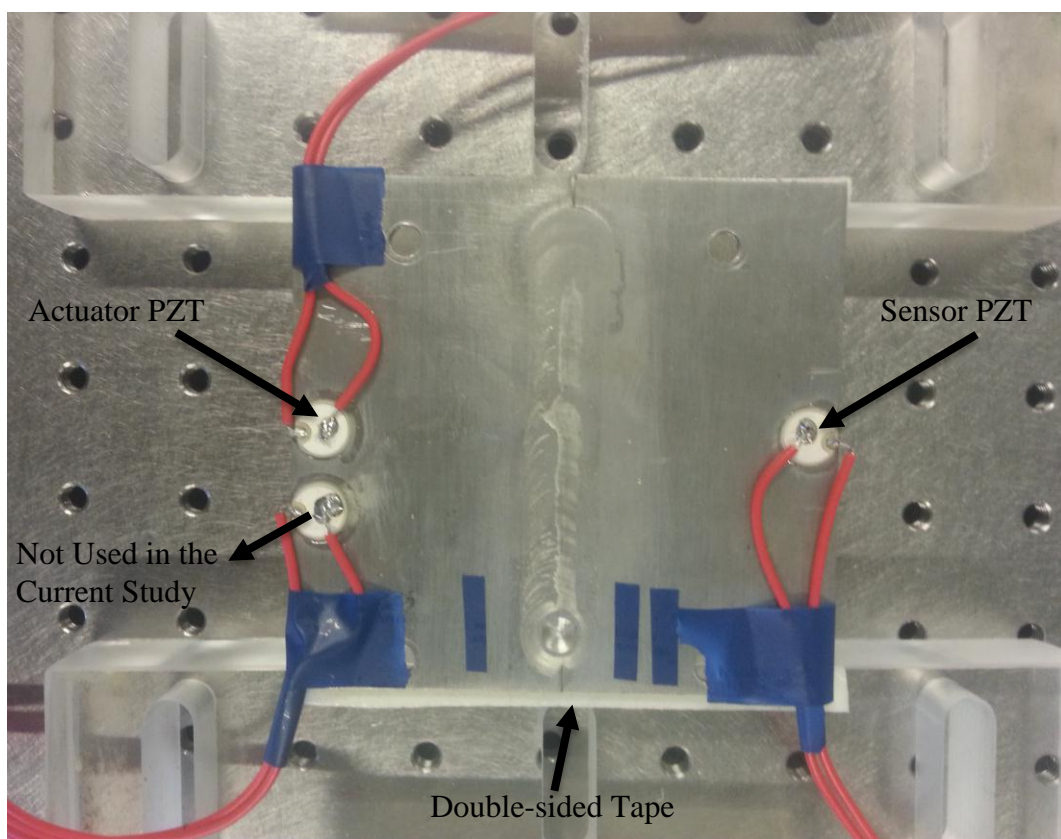


(b)

**Figure 7: (a) A schematic and (b) a real photo of the plates' setup for similar boundary conditions and less noise effects.**

## C. Experimental Variables Control

This section is a separate study that was done to show the effect of non-consistent conditions between different plates.

As a matter of fact, the current experimental setup includes many variables since the experiments are done on 5 different plates. This means that any variation in the plate condition, adhesive quantity and distribution, PZT-plate bond quality, wiring lengths and condition, soldering quantity and quality, sensors position, plate dimensions, temperature and humidity conditions, or in the PZT conditions may lead to a small variation in the response signals. This variation may be in the order of the variation caused by a small defect in the weld.

To study the effect of the variability in such conditions, a sensor network of four PZT elements was placed on a solid plate of the same material and size as the specimens. The PZTs were made to have significantly variable adhesive, soldering, and wiring conditions to study their influence. Figure 8 illustrates the positions of the PZTs and the paths therefore formed between them.

Lamb waves of five different frequencies of 100, 200, 300, 400, and 500 KHz were excited in each path, and the response signals were recorded. The responses of each pair of similar paths were studied; considered pairs were 1-2, 3-4, and 5-6. The amplitudes of three peaks in the first transmission were compared, and the average error was computed. Figure 9 shows the responses of the pair 3-4 at 300KHz and gives an example of the three considered peaks to calculate the error. The arrows point to the three compared peaks. The average errors of the three pairs are reported in Table 3 below. The total average error was 17.27%.

15
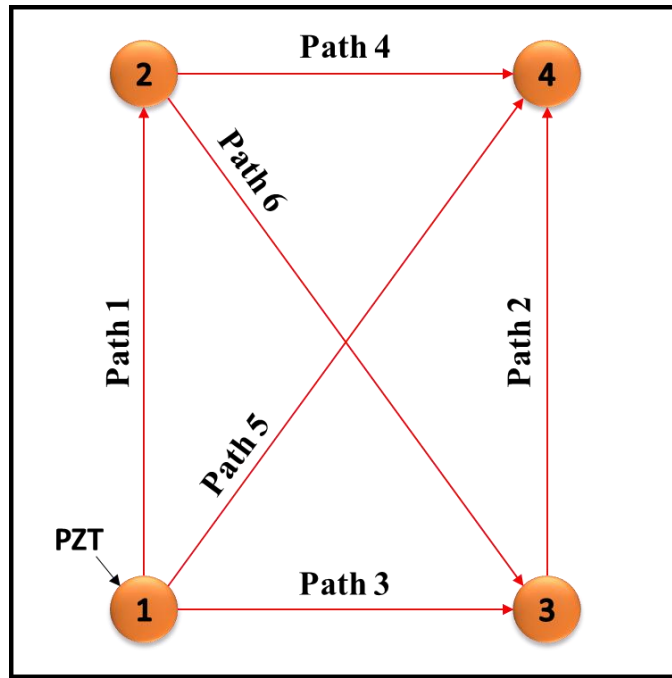
**Figure 8: Variability test sensor network and the formed paths.**
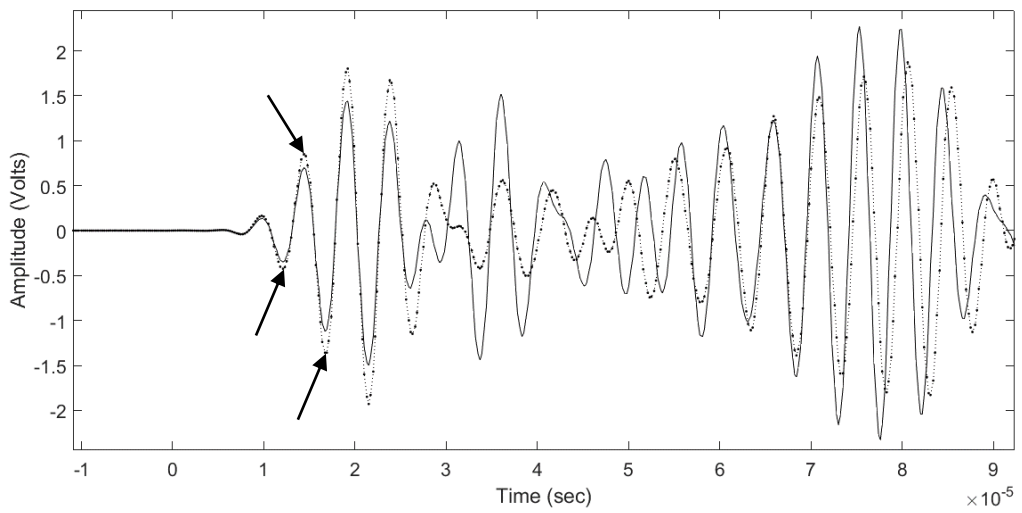


**Figure 9: Variability test between paths 3 (solid) and 4 (dotted) at 200KHz.**

**Table 3: Average errors between pairs of similar paths.**

| Pair | | Average Error (%) | Total Average Error (%) |
|---|---|---|---|
| 1 | 2 | 15.38 | |
| 3 | 4 | 19.64 | 17.27 |
| 5 | 6 | 16.80 | |

This study revealed a recognized effect on the results if the mentioned variables were not well controlled among the testing specimens. An average error of 17.27% should be expected due to non-consistency in the variables between the plates. For this reason, the mentioned variables were tried to be of a good consistency between the five different plates in order to minimize this variability error and have reliable results.

This issue of variability and setup control is to be further studied and discussed in future works.

## D. CT Scans and Finite Element Analysis

The five specimens were scanned using a high resolution CT scanner (Philips Brilliance iCT 256) giving a precision resolution down to 0.335 mm. Figure 10 shows the specimens placed in the CT scanner for scanning. The CT imaging of the specimens had two purposes, the first is to visualize imbedded defects through the welds and know the weld qualities in the tested specimens, and the other purpose is to use the CT images for the 3D reconstruction of the specimens. The 3D models are to be used to validate the experimental results through finite element (FE) simulations.
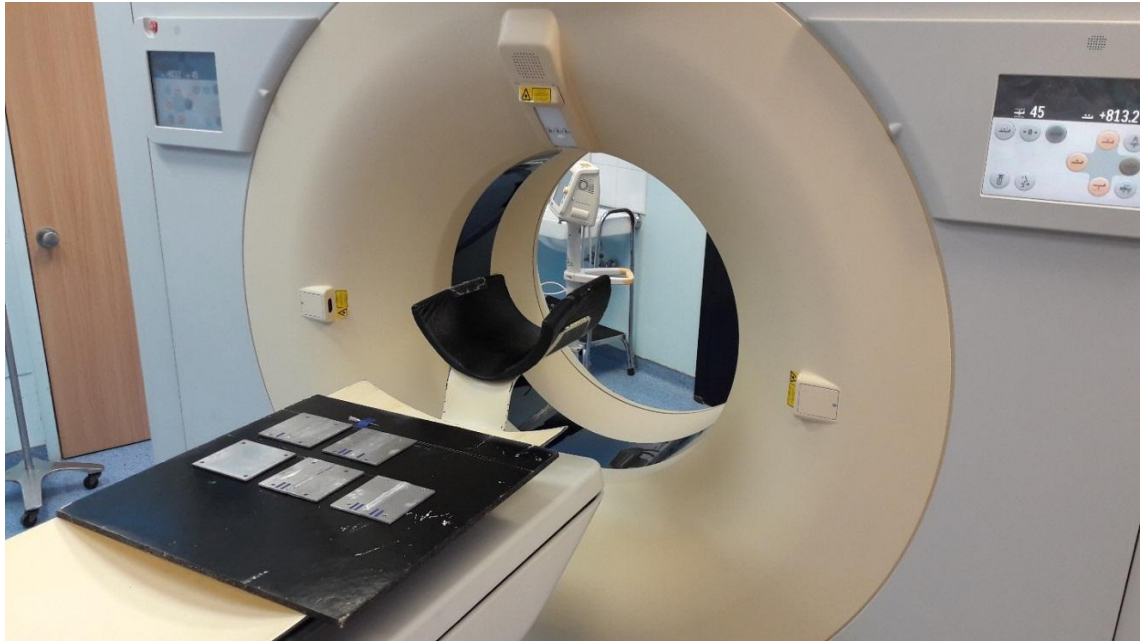
**Figure 10: The five specimens placed in the CT scanner.**

After scanning, the specimens would be arranged in terms of the obtained weld qualities. All the welded plates contained worm holes, but of different sizes and shapes. Figure 11 shows all the plates in the order of numbering mentioned in the experimental setup (again, the numbering was random and not according to any prior expectations). Each plate is shown in two cross sectional views, one perpendicular to the weld direction and in the middle of the plate where the PZTs were placed, and the other parallel to the surface of the plate and passing through the worm hole in its widest section. Plate0 containing no weld is shown also to confirm the continuity in the raw material and the high quality of the CT-scans.

Tapes were used to fix the specimens on a wooden plate to place them in the CT scanner. Those tapes are sometimes visible in the section parallel to the surface of the plate because of the wooden plate's tilted position when performing the CT-scans; the section is on the perfect horizontal so it passes partially through the plate and

partially though the tape. The small tilting angle is obvious in the cross sections
perpendicular to the welds.
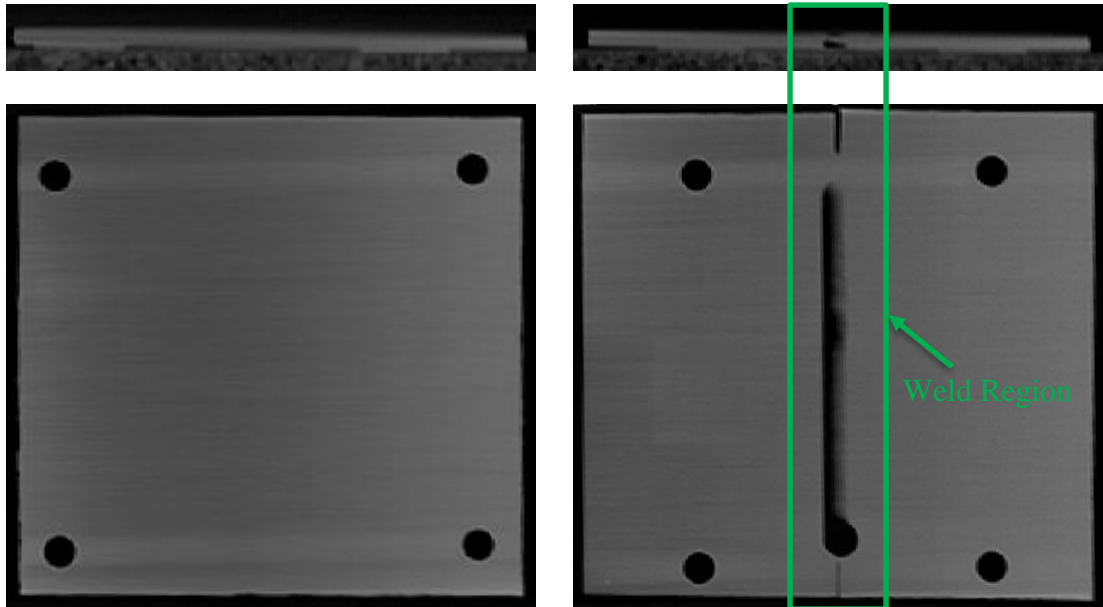


(a)  (b)
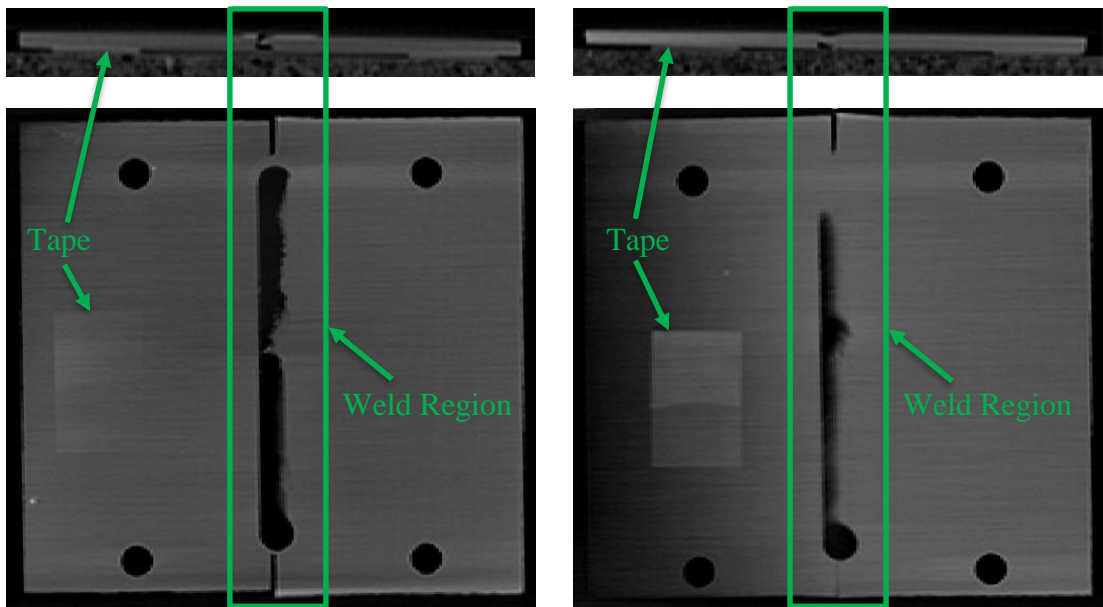
(c)  (d)
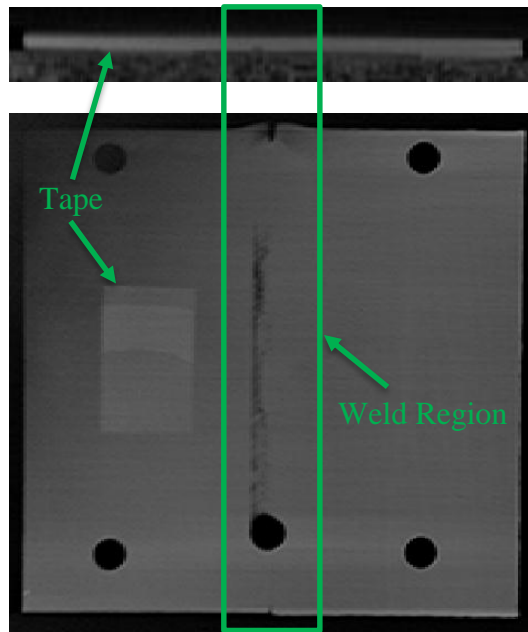
(e)

**Figure 11: Cross sectional views of (a) to (e): Plates 0 to 4 respectively.**

Having those cross sections, it was easy to arrange the specimens in a descending order in terms of their weld quality. This visual arrangement was as follows: Plate0 (with no weld), Plate4, Plate3, Plate1, then Plate2 which was the most damaged one.

### 1. *Creating the 3D Models:*

The next stage was transforming those CT-scans into 3D models on which numerical analysis would be performed. The objective of the numerical simulations is to verify the validity of the approach. The software used for the 3D reconstruction was "Mimics Research 18.0", and the procedure flows as follows:

• Create a mask in a range of certain grayscale thresholds chosen according to the colors of pixels pointing to the plate.

• Use the "Region Growing" option to choose a pixel of the desired plate. This will automatically select all the masked pixels connected to the chosen pixel. A new mask will be created containing the chosen connected pixels only.

• Give the newly created mask the name of the plate.

• Clean the mask slice by slice from all the blurred pixels or the wrong ones due to materials of close illuminance (as the wood and tapes in this case).

• Add two circles to the mask above the top layer, indicating the PZTs, in the same positions where the PZTs were placed in the experimental testing.

• Create a voxel mesh from the finalized mask.

• Export this voxel mesh in a format compatible with the finite element software to be used.

Figure 12 shows the voxel meshes of the five plates which were created using "Mimics". The elements of the voxel mesh were chosen to be hexahedral 8-point elements since they performed better than tetrahedral 4-point elements in the numerical simulations.
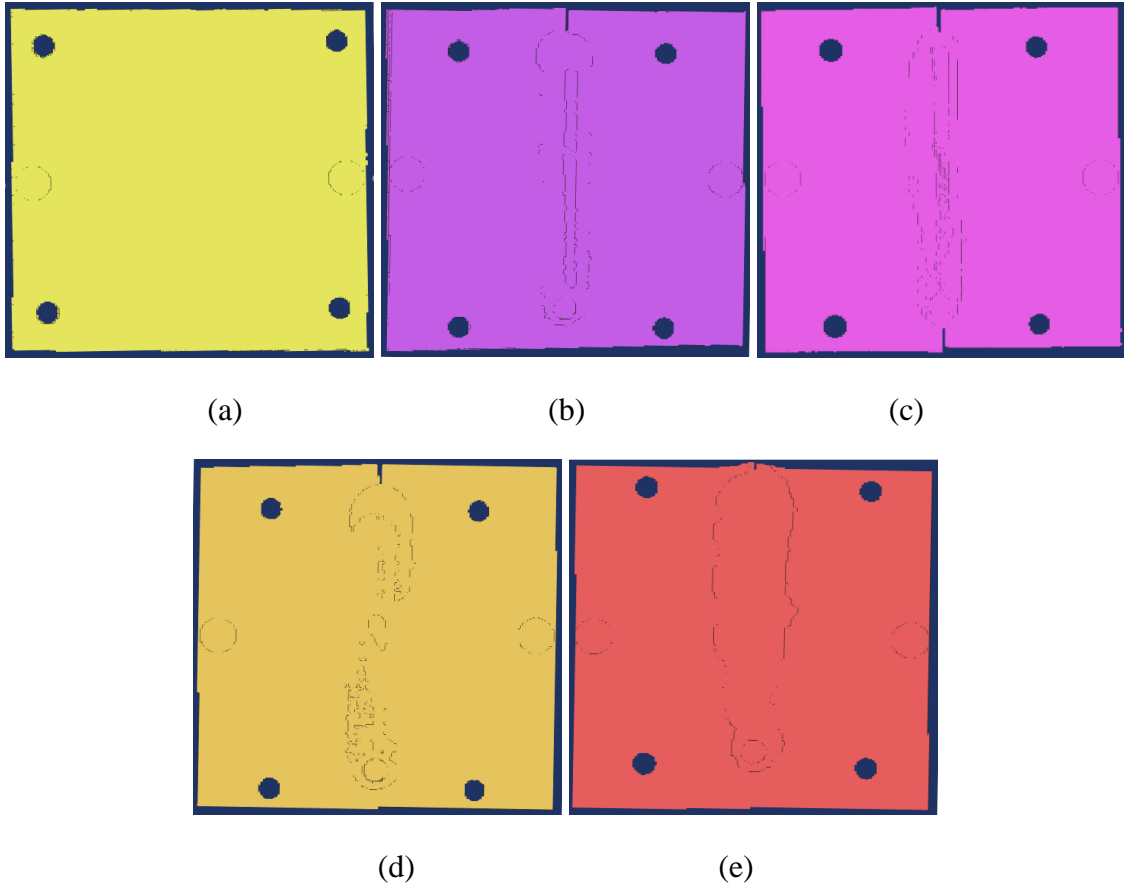
**Figure 12: The five voxel meshes created using Mimics of the five specimens, (a) to (e): Plate0 to Plate4.**

## 2. *Finite Element Analysis*

After creating the 3D models, they were imported into "Abaqus 6.14" and assigned the proper material properties of AZ31B magnesium alloy (Density $= 1.77 g/cm^3$ [51], Modulus of Elasticity $E = 44800\ MPa$ [52], and Poisson's ratio $\mu = 0.35$ [52]). To simulate the performance of the actuator PZT, a cylindrical coordinate system was created in the middle of the actuator, and the peripheral nodes of the actuator were loaded in the radial direction with the same actuating waveforms used in the experiments. The nodes, at the edges perpendicular to the weld direction, were fixed to emulate the boundary conditions of the experiments also. The time history was

22

recorded on a group of 36 nodes of the sensor PZT, and the average response of those nodes was taken for the horizontal displacements in the x-direction (see Figure 13). Figure * shows an example of the loading (the yellow arrows on the right PZT), sensing nodes (the nodes in red on the left PZT), and the boundary conditions (on the upper and lower edges) used for one of the plates (Plate1).
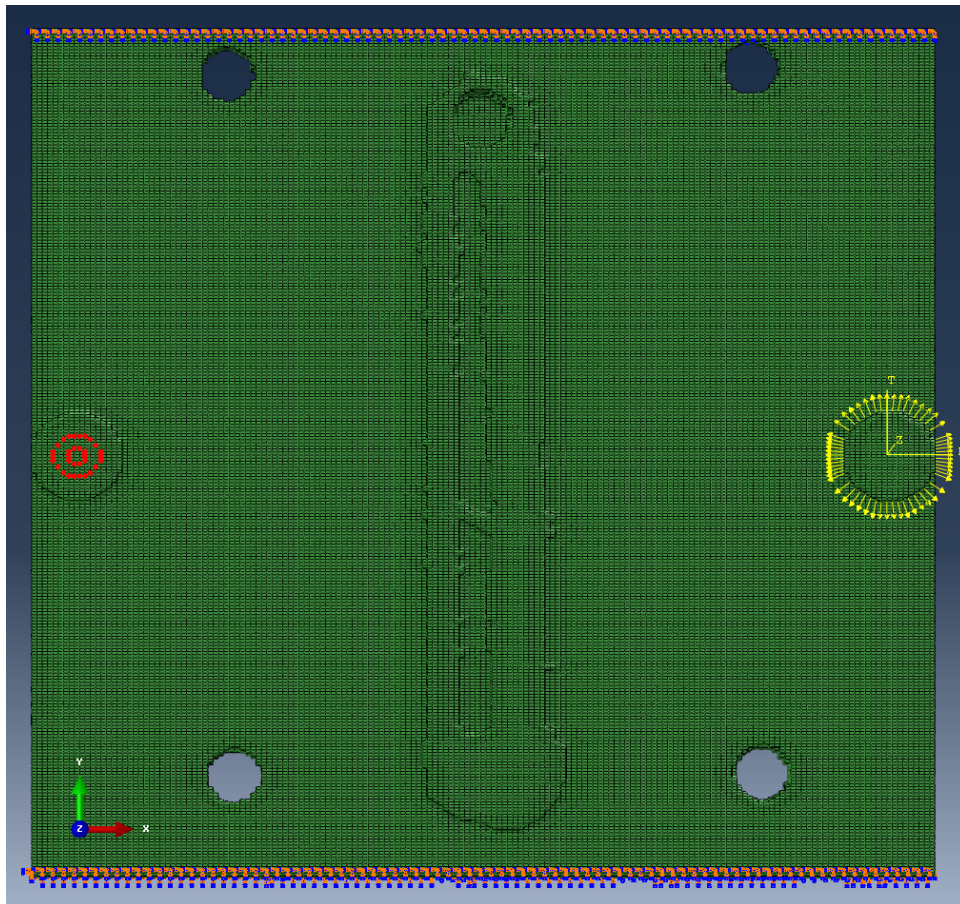


**Figure 13: Sensing nodes (red nodes), boundary conditions (upper and lower edges), and actuator loading (yellow arrows) of the numerical model of Plate1**

## E. Signal processing

### 1. Experimental Raw Data Analysis

The first focus was on the waves propagation behavior and waves characteristics as they interact with magnesium AZ31B alloy plates, with and without flaws. For this purpose, a Matlab based software called "Wavescope", which is developed by the Laboratory for Active Materials and Smart Structures (LAMSS), was used. The program predicts the propagation characteristics for guided elastic waves given the material and structure parameters. Those characteristics include the group velocities, wavelengths, and strains of the symmetric and anti-symmetric wave modes at different frequencies. This helps in identifying and evaluating the possible wave modes in the structure that are suitable for this application. According to "Wavescope" four non-dispersive frequencies were chosen so that only the fundamental anti-symmetric ($A_0$) and symmetric ($S_0$) modes would be excited in the plates. The chosen frequencies were 200, 300, 400, and 500 KHz. Figure 14 and Figure 15 show respectively the results given by "Wavescope" for the expected group velocities and strains of different Lamb wave modes in AZ31B magnesium alloy. The appearing modes are labeled by their names in Figure 14 showing that the chosen range of frequencies excite only the fundamental $A_0$ and $S_0$ modes. The strains shown in Figure 15 give a prior expectation of the ratio between the response amplitudes of the $S_0$ and $A_0$ modes that would appear in the experiments at each frequency. This helps with the group velocities in finding the modes and differentiating them.

24
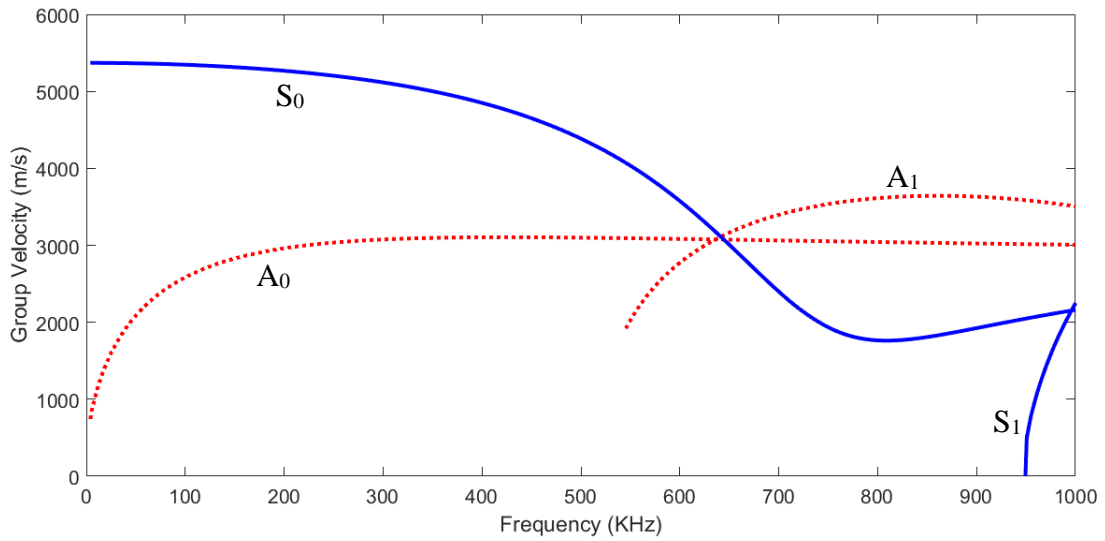
**Figure 14: Expected group velocities of the first four Lamb waves' dispersive modes in AZ31B magnesium alloy given by "Wavescope".**
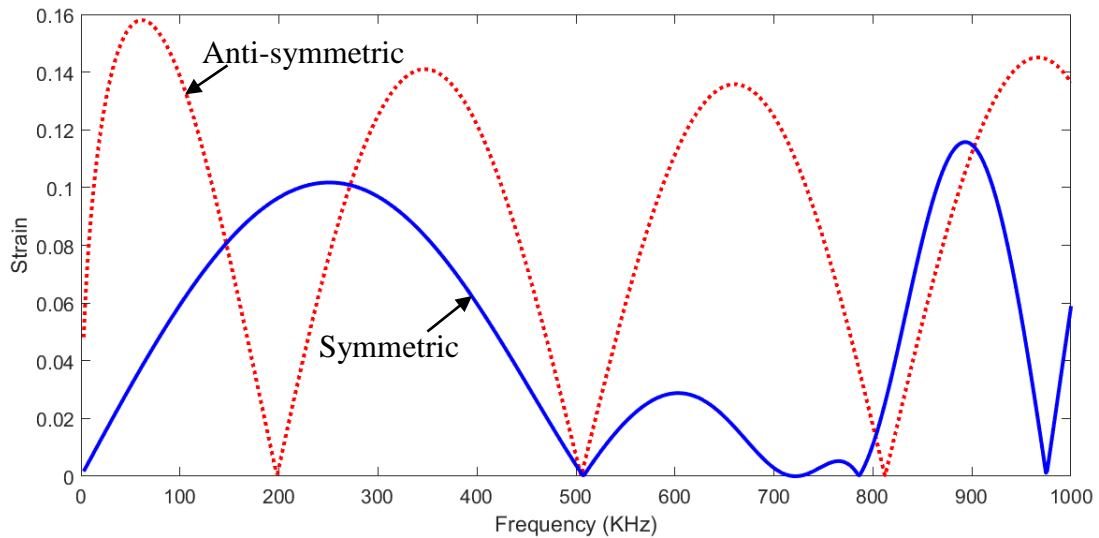


**Figure 15: Expected strain of the symmetric and anti-symmetric Lamb waves' dispersive modes in AZ31B magnesium alloy given by "Wavescope".**

After getting the experimental response waveforms from the sensors, an analysis of the raw data was performed to have some preliminary assessment according the first wave transmissions. The highest peaks' positions were compared to those of the

25

input's highest peaks in order to calculate the velocities of the observed modes. The obtained positions, velocities, and amplitudes were recorded for the 20 obtained signals from the 4 different frequency waveforms sent through the 5 plates (4 x 5 = 20). Velocities were compared to those predicted by "Wavescope" to identify the modes in the first transmissions. Amplitudes were used to compare between the amplitude attenuation and the observed weld quality of each plate.

As an example, Figure 16 shows the normalized input and output signals sensed from Plate0 at an excitation frequency of 200 KHz in the experiments. The dotted curve corresponds to the normalized input signal, while the solid line corresponds to the normalized output signal. The x-coordinate of the highest upper peak in the input, and that of the highest upper peak of the output's first appearing transmission are shown in the gray boxes to the right of the marked peaks. In a simple calculation, the velocity is equal to the distance between the actuator and sensor PZTs (0.09 m) divided by the time difference between the peaks:

$$V_{200} = 0.09/(3.12e^{-5} - 6.3e^{-6}) = 3614.46 \ m/sec \qquad (Eq. 1)$$

According to "Wavescope", the expected group velocity of the $S_0$ mode at 200 KHz is 5268 m/sec, and that of the $A_0$ mode is 2962 m/sec. Unfortunately, the calculated velocity does not match with any of those two values, but it is closer to the velocity of the $A_0$ mode. While the first transmission should be the $S_0$ mode because it is the fastest mode, the highest upper peak doesn't correspond to it.

Due to the fact that lamb waves are highly dispersive in metals and with very high velocities, and because of the small size of the specimens, the modes and their reflections from the boundaries were being superposed. This superposition is building up new peaks of new different positions and amplitudes. For this reason, the sensed

26

waveforms do not show clear mode separation in general, and the signals appear to be very complex. The signals did not give good results on which conclusions can be built.
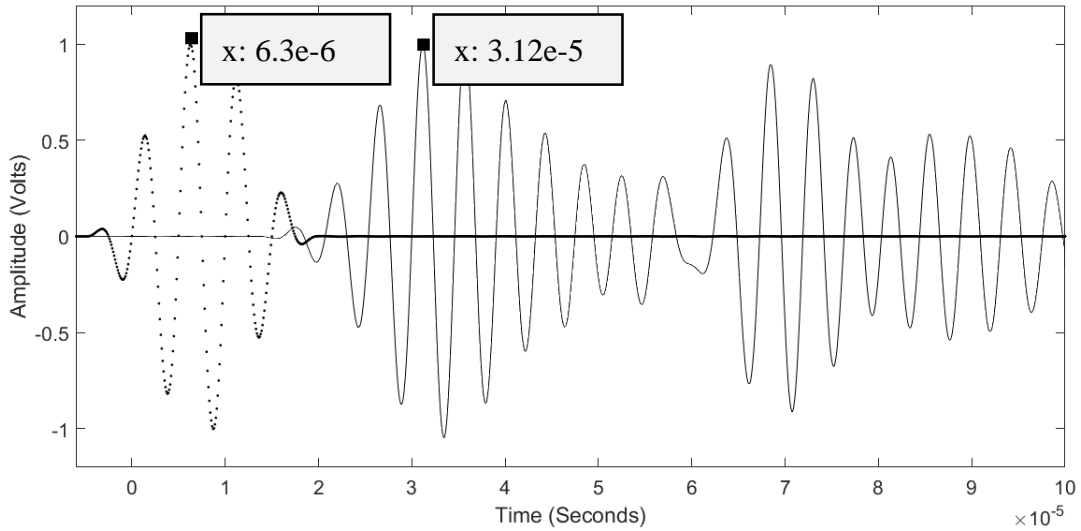


**Figure 16: 200 KHz input and output normalized signals with the highest upper peaks x-coordinates.**

An important advance would be if the modes could be separated by means of some signal processing approaches. Another thing to be considered in the future is repeating the experiments on bigger plates so that better measurements with less complexity may be obtained, hopefully due to the separation of the $A_0$ and $S_0$ modes, and due to the separation of each mode from its reflections as well.

But before going to mode separation, another investigation is worth studying. The $S_0$ mode is known to be sensible for defects lying on surfaces and in thin plates, so the $S_0$ mode was chosen for the investigation. The problem as stated before was that the $1^{st}$ observed pack was not a pure $S_0$ mode, but was a mix of superposed $A_0$ and $S_0$ first transmissions and reflections. For this reason, the $2^{nd}$ upper peak was considered for

27

comparison between responses of different plates. The choice of the 1$^{st}$ upper and lower peaks was omitted because sometimes they may be small and in the order of the noise, so it is not reliable to take one of them as a reference. On the other hand, after the second upper peak, superpositions would have built some new peaks other than that of the first transmission of S$_0$. Consequently, the 2$^{nd}$ upper peak is thought to be a good reference which is more reliable than the others. Table 4 shows the results extracted from the raw experimental data. The table lists, for each frequency, the time of the 2$^{nd}$ upper peak in the input signal, the time and amplitude of the 2$^{nd}$ upper peak in the measured signals, the velocities of the first transmission, and the amplitudes' variation from that of the non-welded plate. An amplitude-based damage index was proposed as follows:

$$DI = \left|V_p - V_0\right|/V_0 \qquad \text{(Eq. 2)}$$

Where:

- $V_p$: the amplitude of the 2$^{nd}$ upper peak of the response signal from the tested plate.

- $V_0$: the amplitude of the 2$^{nd}$ upper peak of the response signal from Plate0 (non-welded).

A statistical summary of the results of the damaged plates among the four frequencies is shown in Table 5. A standard deviation of about 3% was common between the plates "4, 3, and 1" that correspond to medium and low damages, while it increases to about 11 % for the highly damaged plate "2".

28

**Table 4: Results of the raw experimental data.**

| Frequency (KHz) | General & Common Information | | Experimental Results from Raw Data | | | Amplitude Variation | DI |
|---|---|---|---|---|---|---|---|
| | Plate Number | Input's 2nd Upper Pk Time (s) | 2nd Upper Pk Time (s) | Amplitude (V) | Velocity (m/s) | Vp - V0 | abs(Vp - V0)/V0 |
| 200 | 0 | 1.40E-06 | 2.200E-05 | 0.6212 | 4368.93 | 0.000E+00 | 0.000 |
| | 4 | | 2.100E-05 | 0.5683 | 4336.73 | 5.290E-02 | 0.085 |
| | 3 | | 2.190E-05 | 0.5759 | 4390.24 | 4.530E-02 | 0.073 |
| | 1 | | 2.200E-05 | 0.5742 | 4368.93 | 4.700E-02 | 0.076 |
| | 2 | | 2.220E-05 | 0.4364 | 4326.92 | 1.848E-01 | 0.297 |
| 300 | 0 | 1.00E-06 | 2.130E-05 | 0.539 | 4433.50 | 0.000E+00 | 0.000 |
| | 4 | | 2.010E-05 | 0.4886 | 4450.26 | 5.040E-02 | 0.094 |
| | 3 | | 2.110E-05 | 0.4678 | 4477.61 | 7.120E-02 | 0.132 |
| | 1 | | 2.130E-05 | 0.5073 | 4433.50 | 3.170E-02 | 0.059 |
| | 2 | | 2.130E-05 | 0.2976 | 4433.50 | 2.414E-01 | 0.448 |
| 400 | 0 | 7.50E-07 | 2.070E-05 | 0.2143 | 4511.28 | 0.000E+00 | 0.000 |
| | 4 | | 1.955E-05 | 0.207 | 4521.28 | 7.300E-03 | 0.034 |
| | 3 | | 2.050E-05 | 0.1849 | 4556.96 | 2.940E-02 | 0.137 |
| | 1 | | 2.070E-05 | 0.2105 | 4511.28 | 3.800E-03 | 0.018 |
| | 2 | | 2.060E-05 | 0.1004 | 4534.01 | 1.139E-01 | 0.531 |
| 500 | 0 | 6.00E-07 | 2.020E-05 | 0.05762 | 4591.84 | 0.000E+00 | 0.000 |
| | 4 | | 1.905E-05 | 0.05955 | 4607.05 | -1.930E-03 | 0.033 |
| | 3 | | 2.000E-05 | 0.05239 | 4639.18 | 5.230E-03 | 0.091 |
| | 1 | | 2.020E-05 | 0.06358 | 4591.84 | -5.960E-03 | 0.103 |
| | 2 | | 2.000E-05 | 0.02425 | 4639.18 | 3.337E-02 | 0.579 |

**Table 5: Statistical summary of the DIs computed from raw experimental data among the four frequencies.**

| Plate Number | Minimum DI | Maximum DI | Average DI | Standard Deviation |
|---|---|---|---|---|
| 4 | 0.033 | 0.094 | 0.062 | 0.028 |
| 3 | 0.073 | 0.137 | 0.108 | 0.027 |
| 1 | 0.018 | 0.103 | 0.064 | 0.031 |
| 2 | 0.297 | 0.579 | 0.464 | 0.107 |

To make the results of the DI clearer, they will be plotted as bar graphs. The horizontal axis will correspond to the plate name, while the vertical axis will correspond to the DI. The names of the plates will be arranged on the horizontal axis in the ascending order of damage according to what was obtained by the CT-scans (section D). Figure 17 lists the bar graphs, for the four frequencies, of the DI obtained from the raw experimental responses before doing any separation. Figure 18 shows the average

DI of the plates among the four frequencies. The average is presented to show the general trend of the results obtained from the four frequencies. Moreover, averaging is believed to remove errors possibly coming from noise and give a better estimation of the DI.

It was found that the results from the raw data didn't give a precise assessment about the quality of the welds and their right arrangement, therefore, it was necessary to go for a powerful separating technique.
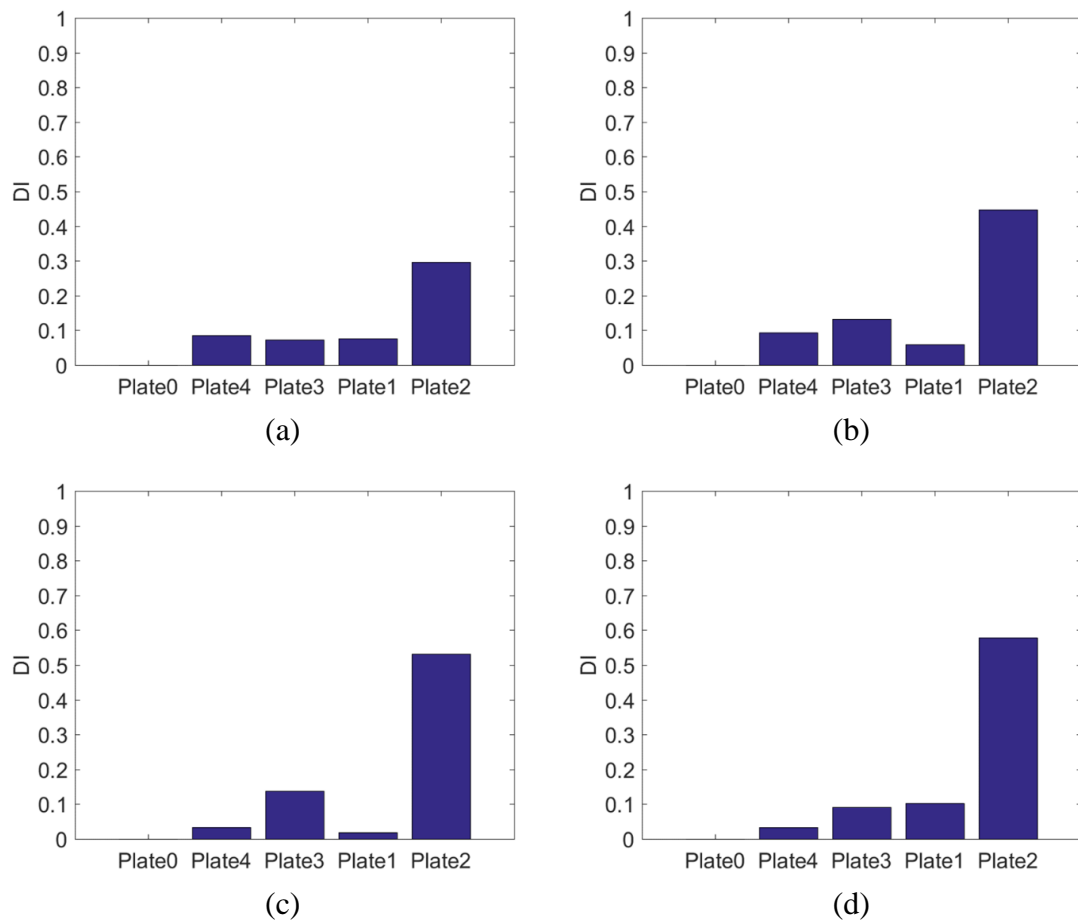


**Figure 17: Damage Index (DI) of the five specimens computed from the experimental responses before separation at (a) 200 (b) 300 (c) 400, and (d) 500 KHz.**
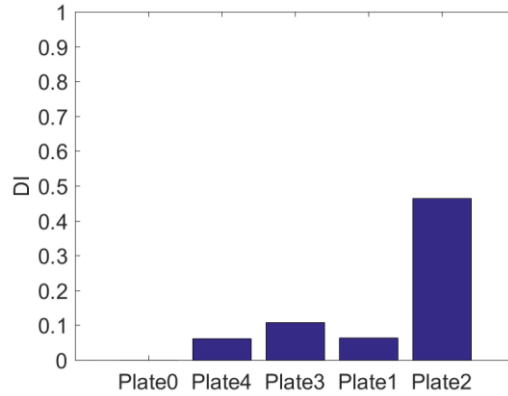
**Figure 18: Average DI among the 4 used excitation frequencies of the five specimens computed from the experimental responses before separation.**

## 2. *Improved CEEMDAN*

In traditional linear time-frequency methods as short time Fourier transform (STFT) and wavelet transform (WT), care should be given to the choice of a previously defined window or a base function before applying. Unlike those methods, empirical mode decomposition (EMD) is totally driven by the data itself. This gives EMD the potential to deal with non-linear and non-stationary signals [53].

EMD is a well-known signal-adaptive separation method which was first proposed by Huang et al. [53]. After that, a series of improvements and adaptations were suggested by several authors to overcome the disadvantages and get better results. Trials of improvements included ensemble EMD (EEMD) [54], Complimentary EEMD [55], complete EEDM with adaptive noise (CEEMDAN) [56], and finally improved CEEMDAN [57]. Improved CEEMDAN was proposed by Colominas et al. [57] and it showed robust separation results with minimum residual errors in comparison to its predecessors. The approach divides the complex signal into several amplitude and frequency modulated functions called modes, where the sum of those modes will build

31

again the original signal with a negligible residual error [57]. Only the initial algorithm referred to as "EMD", and the new algorithm referred to as "improved CEEMDAN" will be stated here for completion.

a. Algorithms

Empirical mode decomposition (EMD) expresses a signal as a totality of amplitude and frequency modulated (AM–FM) functions called "intrinsic mode functions" (IMFs), or modes, plus a last monotonic trend. An IMF signal is defined as a signal having: (1) its number of zero crossings the same as its number of extrema (maxima and minima) or different just by 1; and (2) the mean of its lower and upper envelopes, called local mean, should be equal to zero [57].

*Necessary definitions:*

- $R_k$: is $k^{th}$ the residue of decomposition.

- $\bar{x}$: is the local mean of a signal x.

- $E_k(x)$: is the $k^{th}$ mode of x obtained by EMD.

- $N^{(i)}$: is the $i^{th}$ realization of a white Gaussian noise with zero mean and unit variance.

- $SNR_k$: desired signal to noise ratio between the added noise and the $k^{th}$ residue.

*EMD algorithm:*

- Set $k = 0$ and $R_0 = s$; where $s$ is the signal to be decomposed by EMD.

- Find all the extrema of $R_k$.

- Interpolate among the extrema of $R_k$ to obtain the lower and upper envelopes $e_{min}$ and $e_{max}$.

32

- $\overline{R_k} = (e_{min} + e_{max})/2.$  (Eq. 3)

- $I_{k+1} = R_k - \overline{R_k}$ .  (Eq. 4)

- If $I_{k+1}$ is an IMF:

  - $E_k(s) = I_{k+1}.$  (Eq. 5)

  - $R_{k+1} = x - \sum_{i=1}^{i=k} E_i(s)$  (Eq. 6)

  - $k = k + 1$

  - Go to step 2.

  - Else:

  - $R_k = I_{k+1}$  (Eq. 7)

  - Go to step 2.

- Continue until $R_k$ fulfils a predefined stopping condition (become monotonic for example).

*Improved CEEMDAN algorithm:*

- Set $k = 0$ and $R_0 = s$; where $s$ is the signal to be decomposed by improved CEEMDAN.

- Compute using EMD the local means of $I$ realizations of $R_0$:

$$R_0^{(i)} = R_0 + \alpha_0 E_1(N_0^{(i)})$$  (Eq. 8)

Where:

$$\alpha_0 = \varepsilon_0 . \frac{std(R_0)}{std\left(E_1\left(N_0^{(i)}\right)\right)}$$  (Eq. 9)

And:

$$\varepsilon_0 = \frac{1}{SNR_0}$$  (Eq. 10)

- $\mu_k = Average\left(\left(\overline{R_k^{(i)}}\right)\right) = \frac{1}{I}\sum_{i=1}^{i=I} \overline{R_k^{(i)}}$  (Eq. 11)

- $k = k + 1$.

- The $k^{th}$ mode: $M_k = R_{k-1} - \mu_{k-1}$. $\hspace{4cm}$ (Eq. 12)

- The $k^{th}$ residue: $R_k = R_{k-1} - M_k = \mu_{k-1}$. $\hspace{3cm}$ (Eq. 13)

- Realizations of the $k^{th}$ residue:

$$R_k^{(i)} = R_k + \alpha_k E_1(N_k^{(i)})$$ $\hspace{4cm}$ (Eq. 14)

Where:

$$\alpha_k = \varepsilon_k . std(R_k)$$ $\hspace{4cm}$ (Eq. 15)

And:

$$\varepsilon_k = \frac{1}{SNR_k}$$ $\hspace{4cm}$ (Eq. 16)

- Go to step 3.

- Continue until $R_k$ fulfils a predefined stopping condition (become monotonic for example).

The algorithm is further shown in a flowchart in for more clarity.
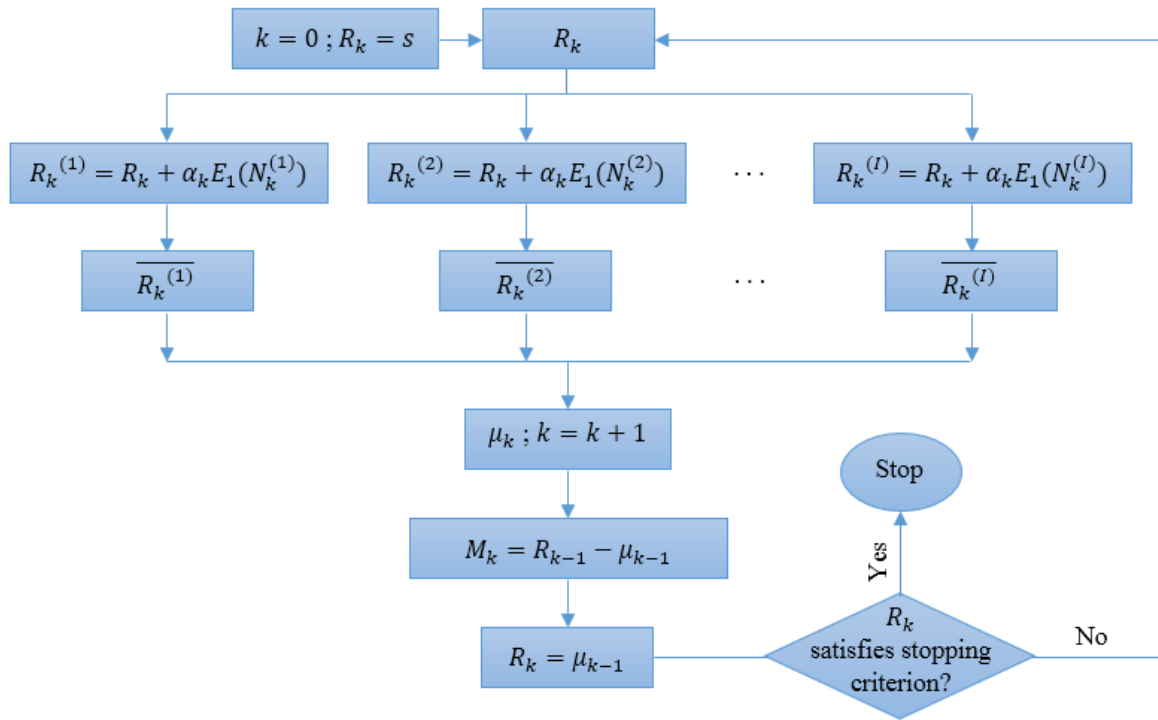
**Figure 19: Flowchart of the algorithm of improved CEEMDAN**

b.  Separation Example

As an example, Figure 20 shows the 10 modes obtained by improved CEEMDAN when decomposing the same response signal that was shown in Figure 16. The complete original signal is shown in Figure 20 (a). The horizontal axes correspond to time (in seconds), and the vertical axes correspond to the amplitude (in volts). A quick look on the order of amplitudes in comparison to the original signal, shows that the second and the third modes are the most relevant ones since they have the highest orders which are the same as that of the original signal. The convenience in the second mode is that it has approximately the shape of the input signal which is a desired result. Unfortunately, not all the decomposed signals had led to such a suitable result for the $S_0$ mode. Different Lamb wave modes were separated from each other, but the reflections of the mode itself were stuck to the mode. This made the choice of the 2nd upper peak

for comparison between responses of the different plates is still the most convenient

choice before the reflections start to build up new wrong peaks.
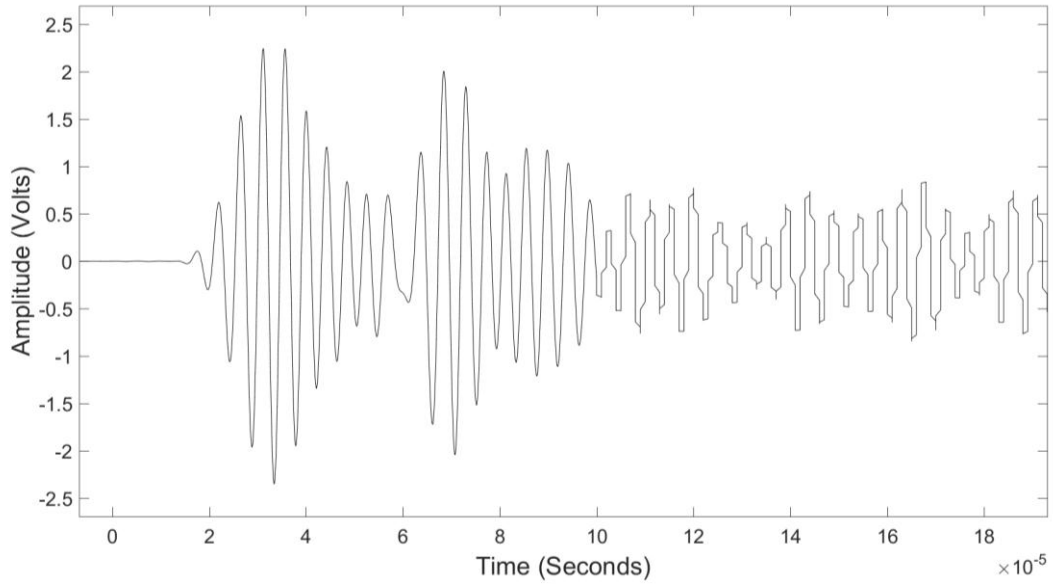


(a)
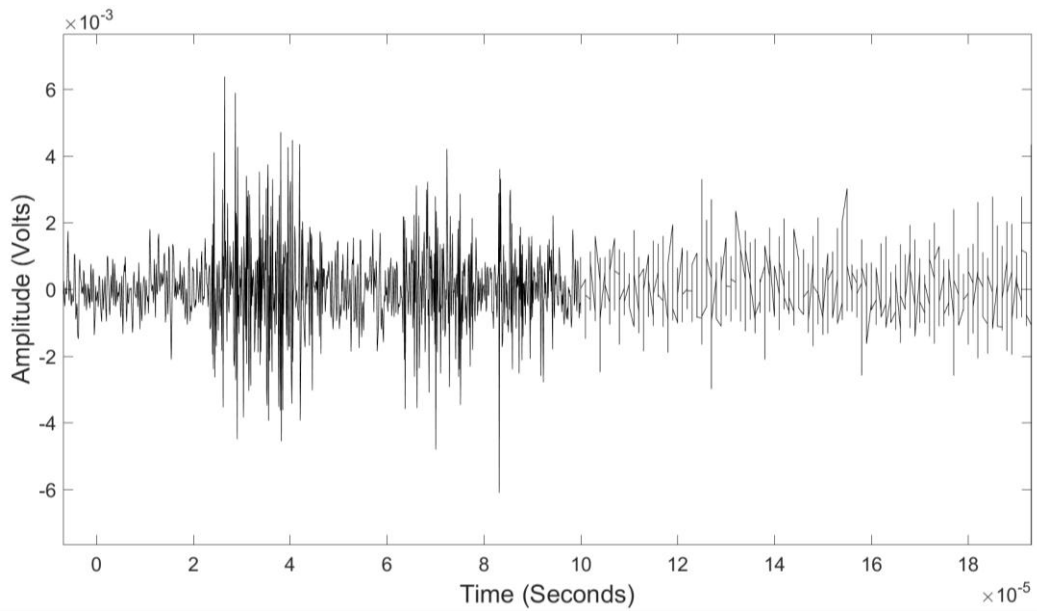


(b)
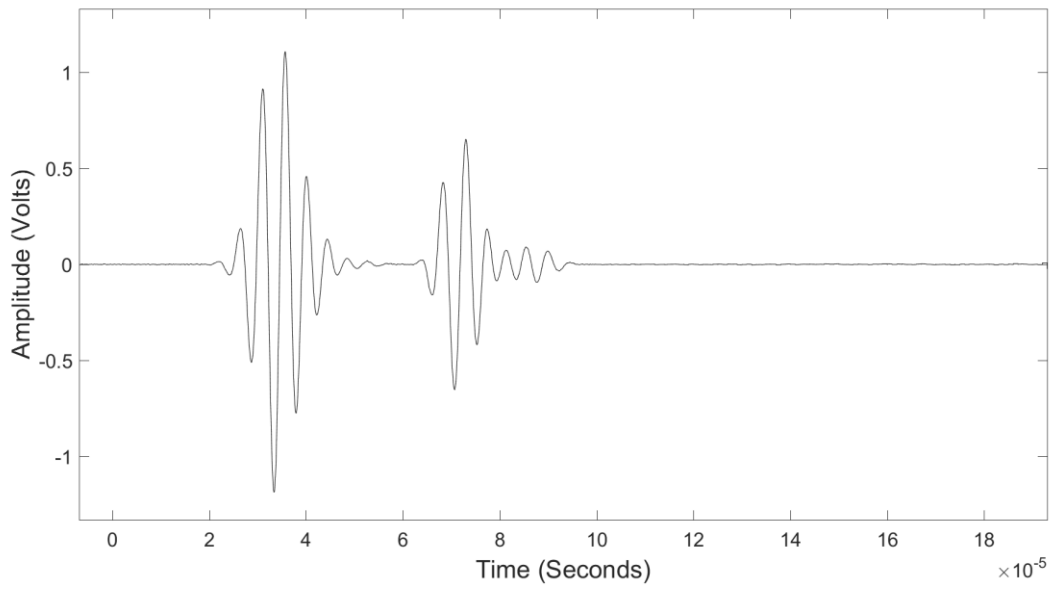
(c)
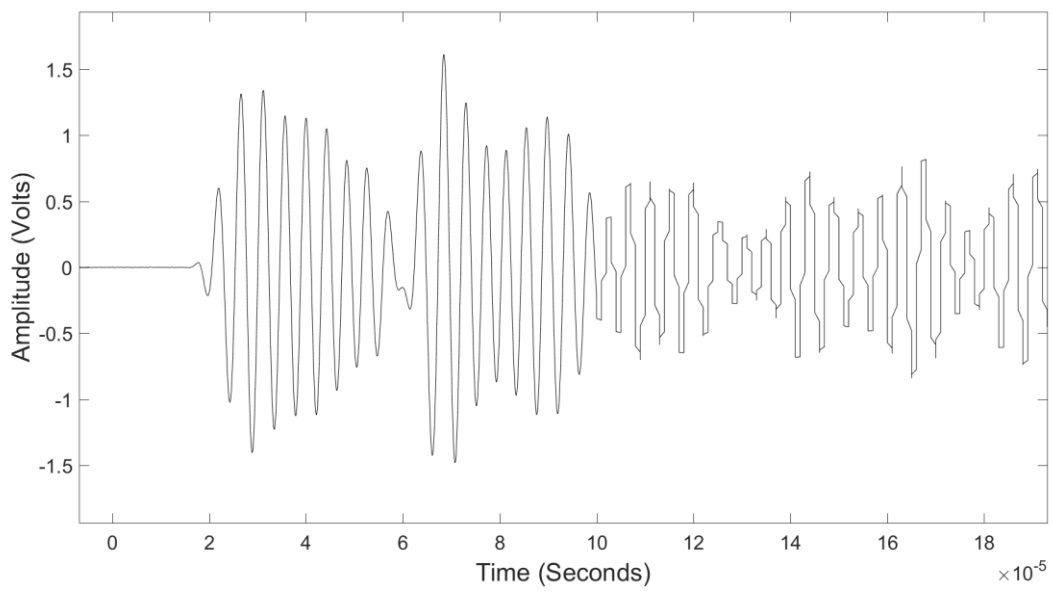


(d)
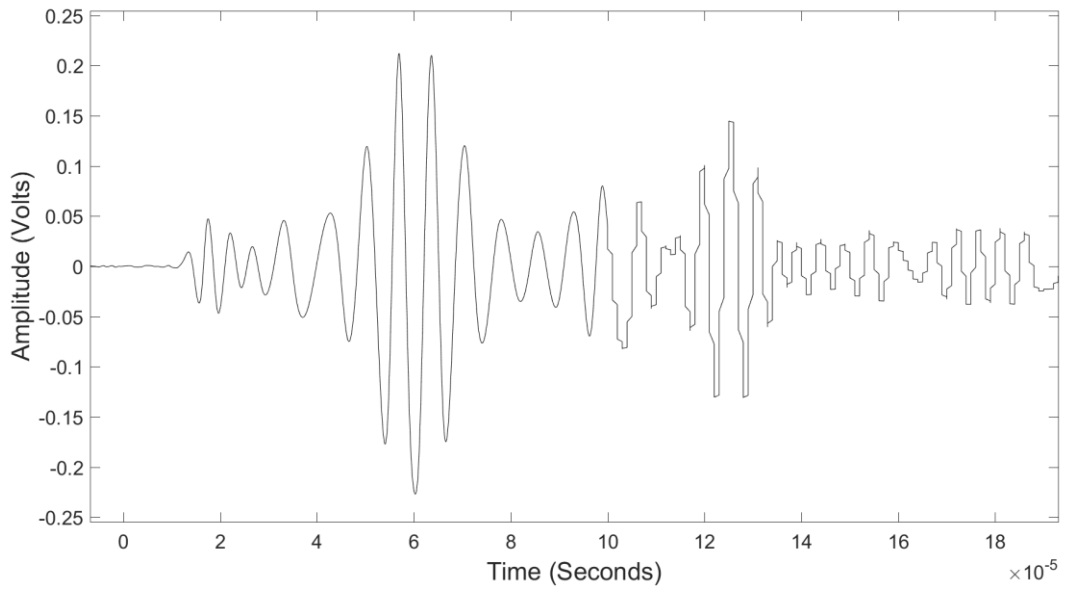
(e)
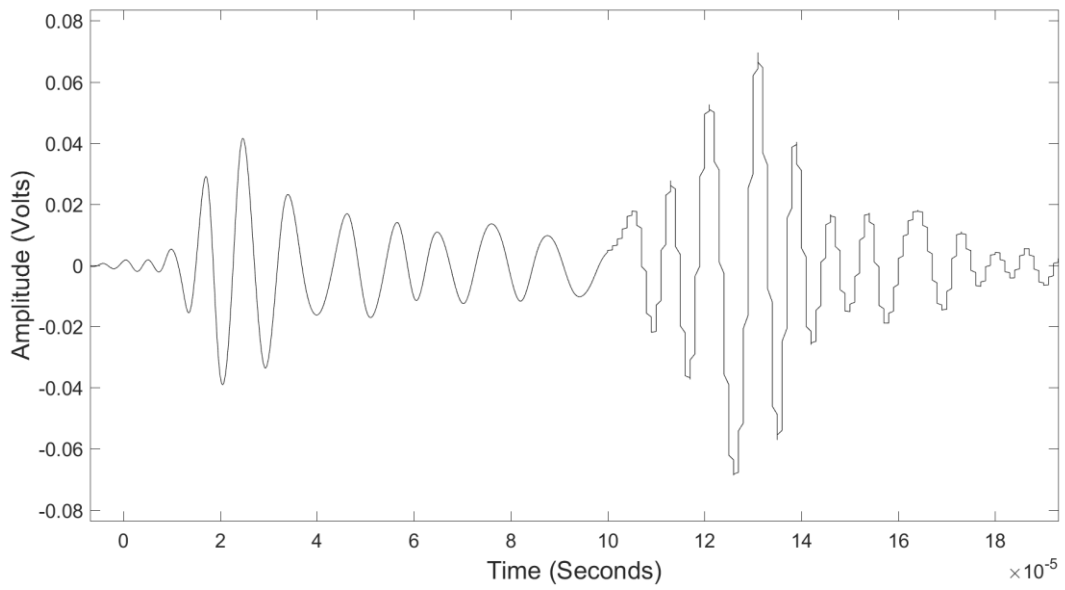


(f)
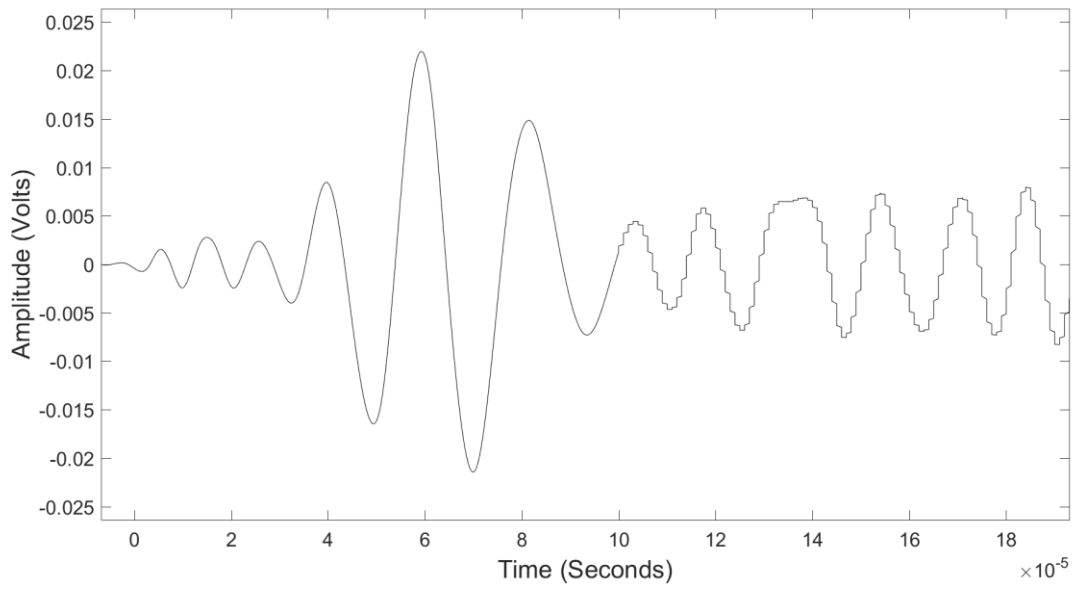
(g)
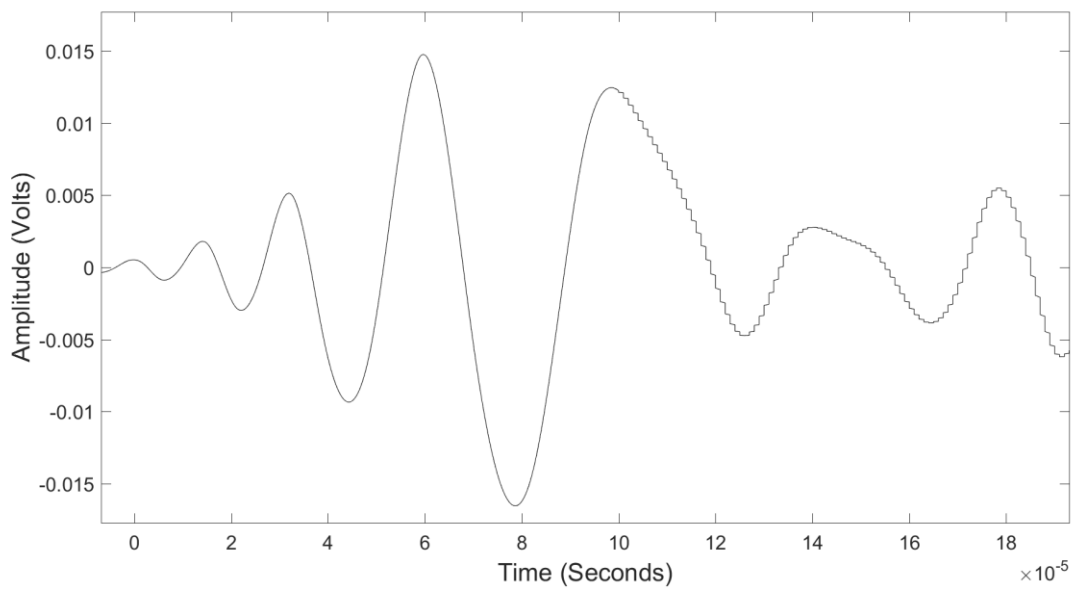


(h)
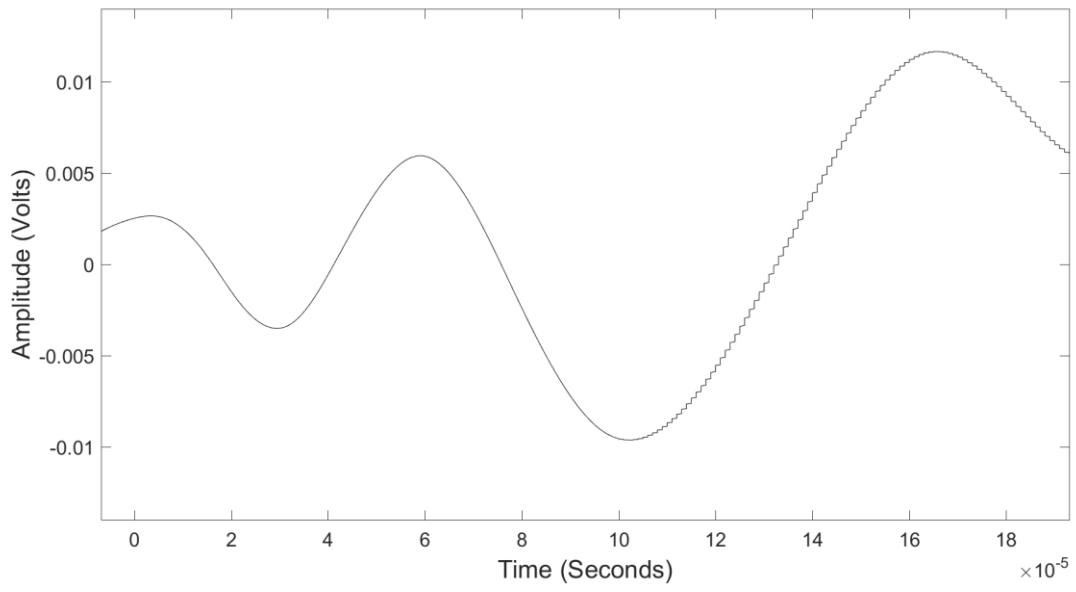
(g)
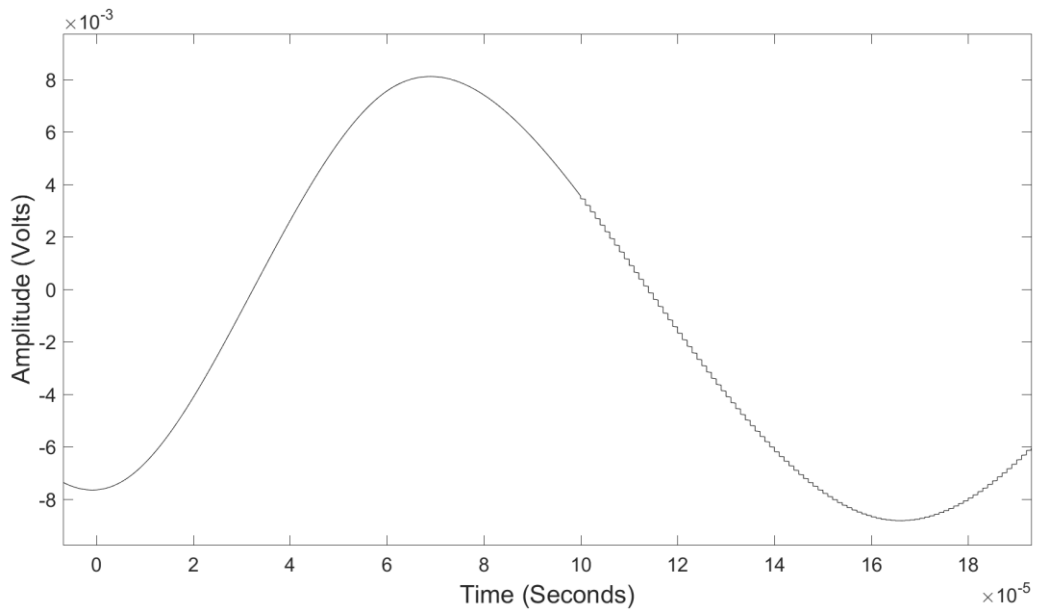


(i)
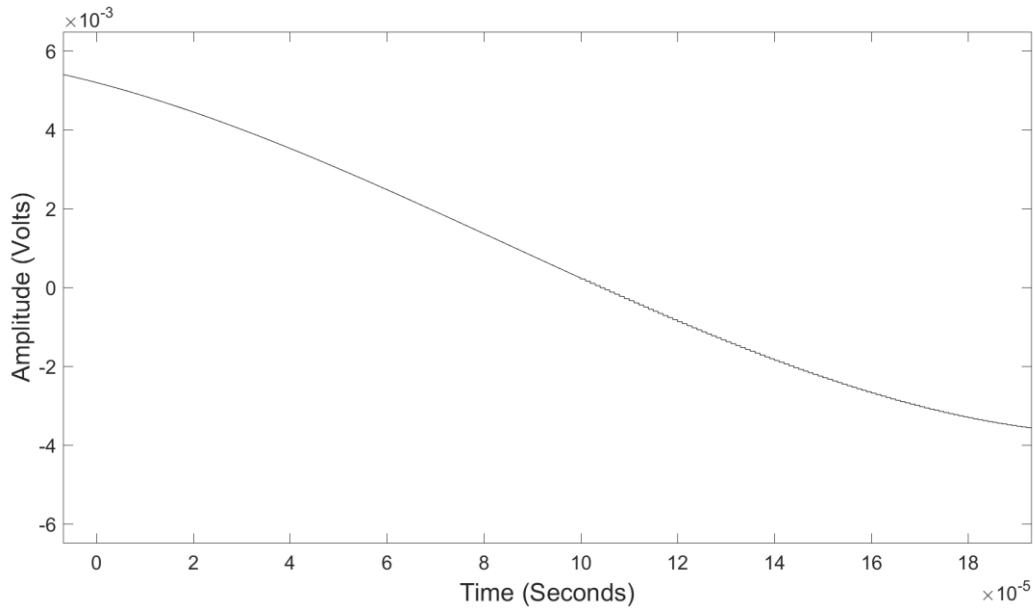
(j)

**Figure 20: (a) The original 200 KHz response signal of Plate0, (b) to (j): the 10 obtained modes after the separation of the signal using Improved CEEMDAN.**

## 3. *Results After Separation*

Response signals from both experimental testing and FE simulations were separated using improved CEEMDAN. The $S_0$ modes were chosen according to their velocities and order of amplitudes in comparison with the original signals. The choice of the $S_0$ mode was ensured using the results of "Wavescope". Then the amplitudes of the 2nd upper peaks were used to calculate the DI for each plate at each of the four chosen frequencies (200, 300, 400, and 500KHz).

For the experimental measurements, the DIs for different plates were consistent with the weld qualities as a general trend, but with some errors between the plates of comparable weld qualities (Plate1 and Plate3). Plate 4 kept an approximately constant DI among the 4 frequencies, while Plate 1 varied significantly for only one frequency. However, Plate 3 alternated noticeably between different frequencies. Those variations

41

may be probably explained that the level of noise is of the same order as the variations in the response due to the close-size-defects. On the other hand, the very bad weld in Plate 2 was always detected clearly because of its response's big variation from the other plates (see Figure 21). Figure 22 shows the average DI of each of the five specimens among the 4 used excitation frequencies. The average DI totally agrees with the actual weld qualities given by the NDE, thus arranging the plates in the descending order of damage as Plate0, Plate4, Plate3, Plate1, then Plate2.

The results obtained do not show a lot of variability limitation (explained in section C) since the overall outcome was in total agreement with the actual weld qualities (Figure 22). This means that the setup variables were very well controlled between the plates.

From another side, the numerical simulations kept the same arrangement among all the 4 frequencies. Figure 23 and Figure 24 present respectively the DI of each of the five specimens for the 4 excitation frequencies, and the average DI of the specimens among the 4 frequencies. The classification according to the proposed DI totally agreed with the observed qualities of the welds. This proves the validity of the method for assessment of welds in thin plates and reveals the sensitivity of the $S_0$ mode of Lamb waves to FSW defects.
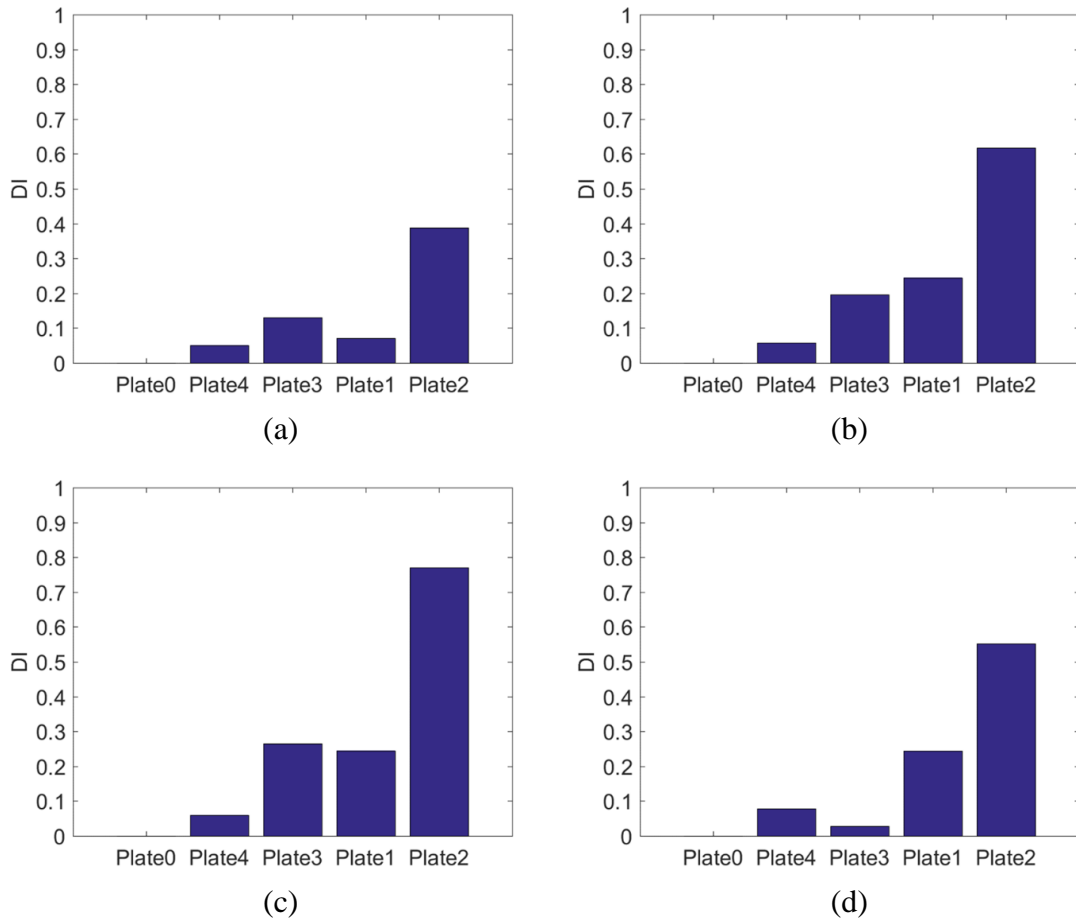
**Figure 21: Damage Index (DI) of the five specimens computed from the experimental responses after improved CEEMDAN separation at (a) 200 (b) 300 (c) 400, and (d) 500 KHz.**
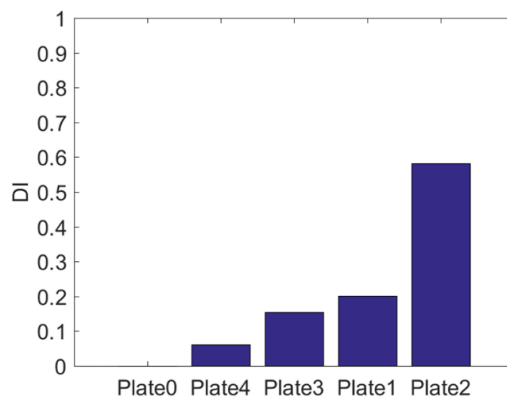


**Figure 22: Average DI among the 4 used excitation frequencies of the five specimens computed from the experimental responses after improved CEEMDAN separation.**
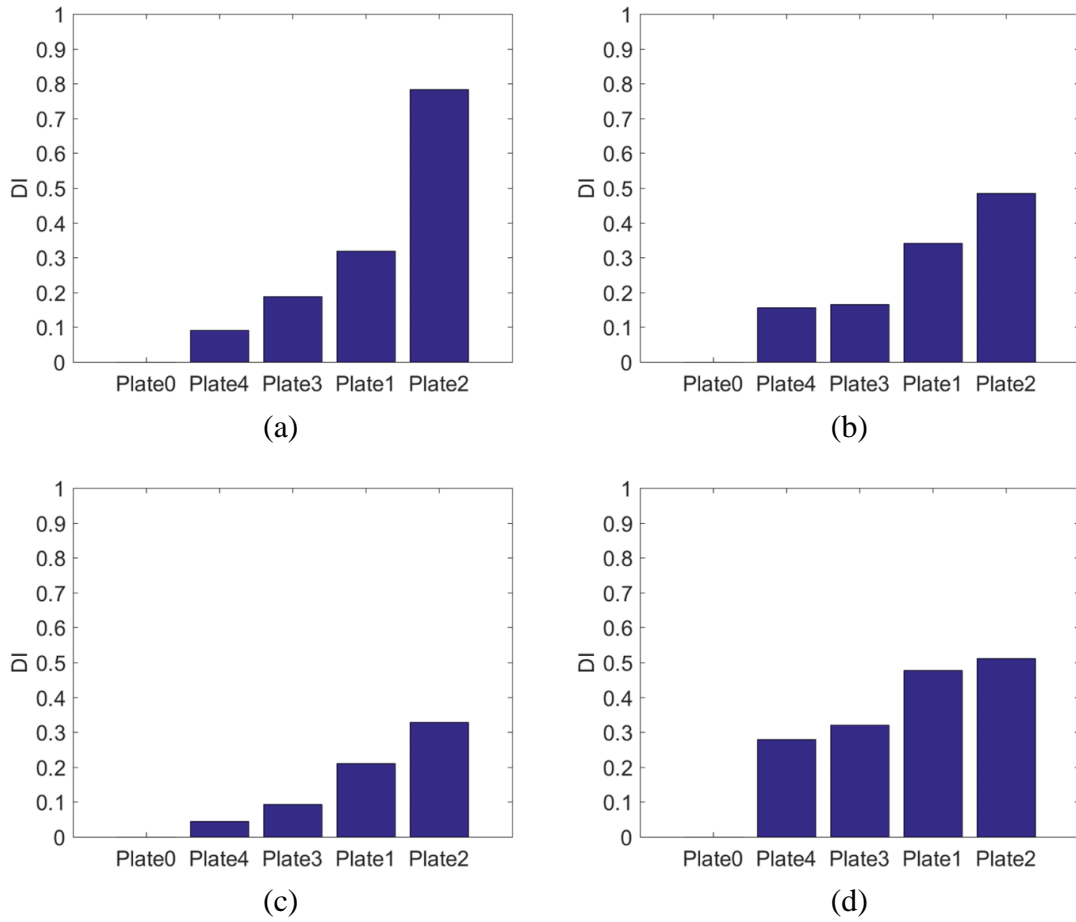
**Figure 23: Damage Index (DI) of the five specimens computed from the numerical responses after improved CEEMDAN separation at (a) 200 (b) 300 (c) 400, and (d) 500 KHz.**
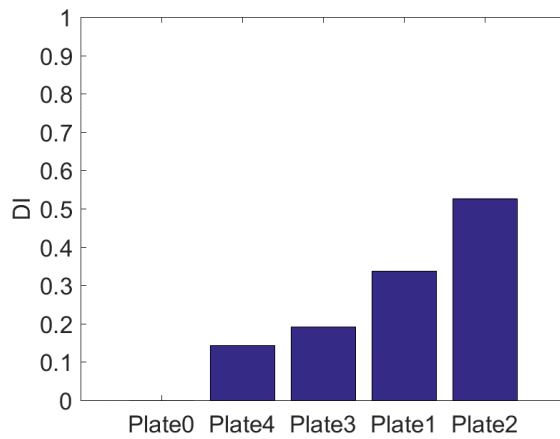


**Figure 24: Average DI among the 4 used excitation frequencies of the five specimens computed from the numerical responses after improved CEEMDAN separation.**

Table 6 and Table 7 list the statistical properties of the variations of the DIs of the plates with the change of the excitation frequencies, respectively, for the experimental and FEA results after separation by improved CEEMDAN.

The standard deviation ranged from 1% for Plate4 of the smallest damage size to 13.7 % for Plate2 of the greatest damage size in the experimental separated data. While the FEA separated data showed a higher variation between different frequencies where the standard deviation ranged from 8.2% to 16.3%.

**Table 6: Statistical summary of the DIs computed from separated experimental data among the four frequencies.**

| Plate Number | Minimum DI | Maximum DI | Average DI | Standard Deviation |
|---|---|---|---|---|
| 4 | 0.051 | 0.078 | 0.061 | 0.010 |
| 3 | 0.027 | 0.265 | 0.154 | 0.088 |
| 1 | 0.071 | 0.245 | 0.201 | 0.075 |
| 2 | 0.388 | 0.770 | 0.582 | 0.137 |

**Table 7: Statistical summary of the DIs computed from separated FEA data among the four frequencies.**

| Plate Number | Minimum DI | Maximum DI | Average DI | Standard Deviation |
|---|---|---|---|---|
| 4 | 0.045 | 0.279 | 0.143 | 0.088 |
| 3 | 0.094 | 0.321 | 0.192 | 0.082 |
| 1 | 0.211 | 0.477 | 0.337 | 0.094 |
| 2 | 0.329 | 0.783 | 0.527 | 0.163 |

As a matter of fact, waves of a different wavelengths react differently with a certain damage depending on the size of the damage compared to that of the wavelength. Of course, a wave passing through the damage more than once (with a small wavelength), for example, will be affected by the damage more than a wave that

45

just jumped above it (with a big wavelength). For this reason, this variation between different frequencies is expected since a wave of a different frequency is of a different wavelength. This is one reason that studies are done to choose the most convenient working frequencies for each specific application.

As for this application, the 300KHz excitation frequency have given the best precision for the experimental measurements, but according the FEA results, all the four frequencies may be used for a similar examination. Therefore, 200, 300, 400, and 500 KHz are suggested as convenient working frequencies for testing AZ31B magnesium alloy plates of 3 mm thickness.

a.  Damage Size and DI: A Comparison

It is important for a damage detection approach to be able of quantifying the detected damage. For this sake, the DI results of 300KHz frequency will be compared with the volume of the damage ($V_d$). The volume of the damage was calculated using "Mimics" models in a region of 30.5 mm around the sensing path as illustrated in Figure 25. The calculated damage volumes are listed in Table 8. The Plates are arranged in the ascending order of weld quality (found in section D) to support this finding again using the calculated volume of the damage.
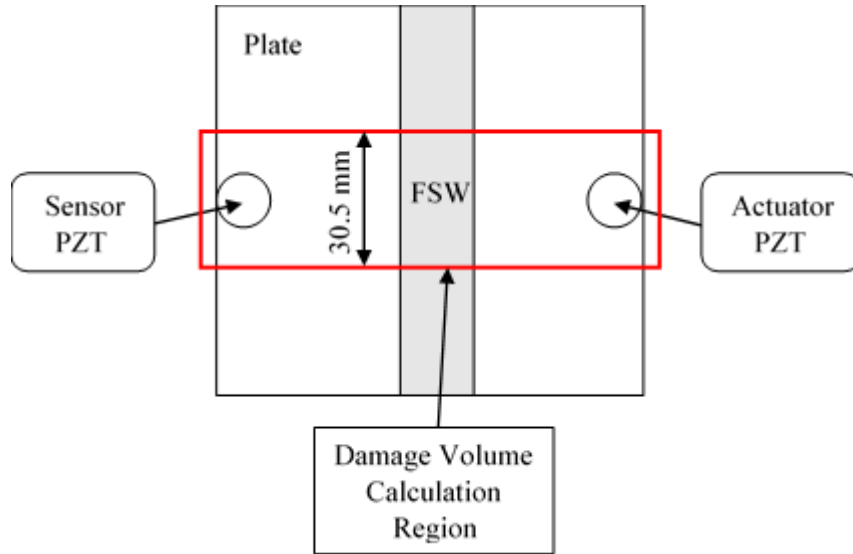
**Figure 25: Illustration of the region within which the damage volume was calculated.**

**Table 8: Damage volumes and damage ratios of the four damaged plates.**

| Plate Number | Width of Measurement Region (mm) | |
|---|---|---|
| | 30.5149663 | |
| | $V_d$ = Damage Volume (mm$^3$) | $R_d = V_d$ / Plate Thickness |
| 4 | 43.175 | 1.609 |
| 3 | 113.089 | 4.214 |
| 1 | 143.089 | 5.331 |
| 2 | 202.960 | 7.562 |

The realtion between the damage volume and the DI is expected to be linear, so a regression line was fitted for both the experimental DI and the DI computed from FEA. The DIs are plot against the damage volume of each plate in Figure 26. The regression parameters were calculated using a "Matlab" buit-in function, and the two lines are shown also in Figure 26. The equations of the experimental regression line and the FEA regression line were found to be very close and are respectively:

$$Experimental\ DI = 0.0024 \times V_d \qquad \text{(Eq. 17)}$$

47

$$FEA\ DI = 0.0023 \times V_d \qquad \text{(Eq. 18)}$$
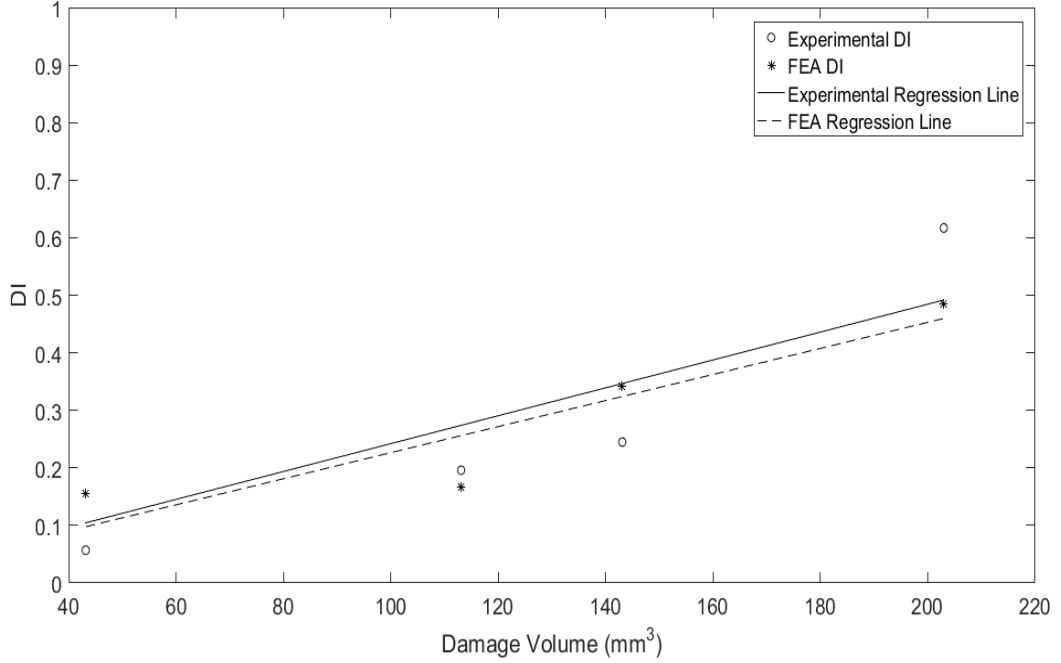


**Figure 26: Experimental and FEA DIs and the fitted regression lines.**

In fact, the thickness of the plate plays an important role in the propagation behaviour of a Lamb wave. This also makes an effect of the thickness on the reaction between the Lamb wave and an imbeded damage. The linear relation between the DI and the damage volume is then expected to be as follows:

$$DI = a \times \frac{V_d}{Plate\ Thickness} = a \times R_d \qquad \text{(Eq. 19)}$$

$R_d$ is also shown in Table 8 for each plate, where the thickness of the plate is 3 mm. This makes the proposed relations for the experimental and FEA results respectively as follows:

$$Experimental\ DI = 0.0072 \times R_d \qquad \text{(Eq. 20)}$$

48

$$FEA\ DI = 0.0069 \times R_d \qquad\qquad\text{(Eq. 21)}$$

This is a proposed linear relation which needs more investigations and an indepth study to be validated. It is not expected to give a precise quantification of damage rather than a rough value to get an idea about the severity of damage. Moreover, it is not expected to be a general relation, but a relation for this specific kind of material (AZ31B magnesium alloy). To try this, a case study will be addressed in the following section.

b. Case Study

FSW AA7020-T651 aluminum alloy plates were imported from the French manufacturer "Groupe TRA-C industrie". Those plates are of different weld parameters and of dimensions 300 x 300 x 5 mm. They were CT-scanned to visualize the qualities of the welds, and one plate was found to have a worm hole defect along the weld. The sections of the damage in the plate are shown in Figure 27.

The experimental DI of this plate was calculated in comparison with the response of another non-defected similar plate. The predicted damage volume was then computed according to equation (Eq. 20). The damage volume was determined from the CT-scans using "Mimics" software, and the error of damage prediction was finally calculated. The results are shown in Table 9.

The damage volume was predicted with an error of less than 12% using the proposed equation (Eq. 20). Although it is an acceptable error, this equation still needs validation and more amelioration in future studies.

On the other hand, a training technique is believed to be the most convinient way to get a valid and a powerful prediction. If training was applied for a certain

49

application, the DI may be used for predicting damage sizes in newborn and in-use

FSW plates aw well.
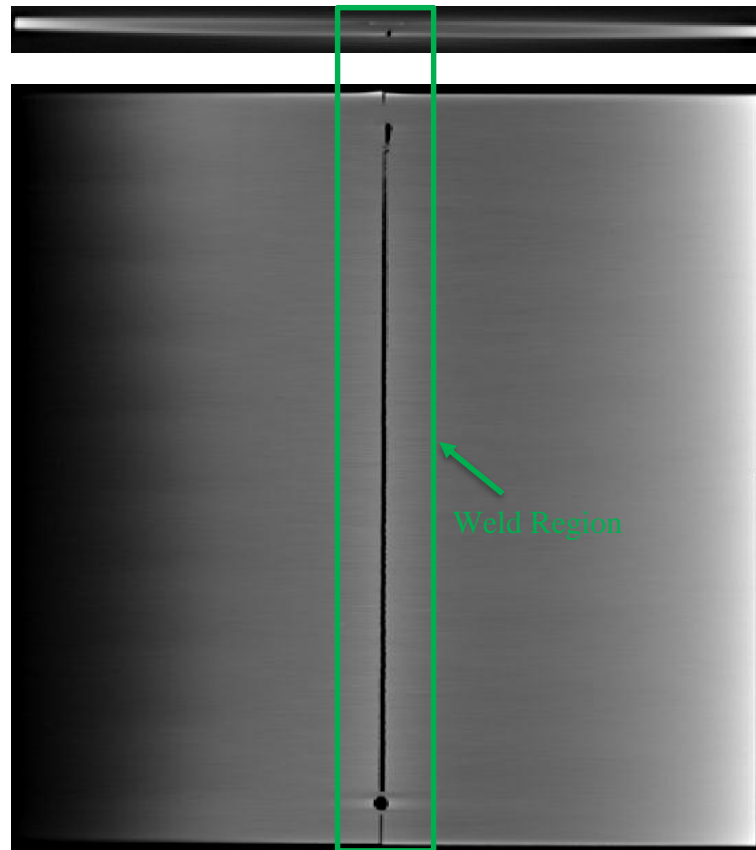


**Figure 27: Cross sectional views of the damaged AA7020-T651 aluminum alloy friction-stir-welded plate.**

**Table 9: Damage volume prediction results.**

| Experimental DI | Predicted $R_d$ = <br> Experimental DI / 0.0072 | Predicted $V_d$ (mm$^3$) = <br> Predicted $R_d$ x Plate Thickness |
|---|---|---|
| 0.247 | 34.373 | 171.866 |
| Measured Damage from CT-scans using Mimics | | Prediction Error (%) = |
| Width of Measurement Region = 30.485 mm | | |
| $V_d$ = Damage Volume (mm$^3$) | | 100 x Abs(Predicted $V_d$ - $V_d$ ) / $V_d$ |
| 194.965 | | 11.85 |

# CHAPTER III

# BVID DETECTION AND ASSESSMENT IN COMPOSITE SANDWICH STRUCTURES

## A.  Introduction

Considering the need for light, nonmetallic materials while maintaining the desirable properties of metals, composite materials appear to be the most convenient metal substitute by virtue of their high strength-to-weight ratio, flexibility in design, and corrosion and fatigue resistance. Composite materials are now the primary materials used in the aerospace and aeronautical industries. They are prone to various forms of damage, including fiber breakage, matrix cracking, delamination, and barely visible indentation damage (BVID). BVID can be caused by a low velocity impact resulting from runway debris or even small birds during landing, takeoff, or taxiing, dropping tools [58] during maintenance or assembly, passenger boarding ramps, or other ground support equipment [59]. BVID can result in a noticeable decrease in the load-carrying capability of the material [60] and such damage can develop progressively, leading to a catastrophic failure [61].

Much research has focused on evaluating BVID in composite and metallic structures. Mustapha et al. [6] studied the characteristics of guided waves and their interaction with tapered sandwich structures with foam core. They proposed algorithms for the detection and localization of multiple defects using an active sensor network. Further, Mustapha et al. investigated the use of ultrasonic guided waves to detect BVID in CF/EP sandwich composites. They presented two algorithms based on the time reversal method and a wave attenuation-based method, respectively [7]. Ruzek et al.

[62] compared the performance in composite sandwich structures of three damage detection techniques: visual inspection, C-scan and shearography. They found that visual inspection lacked effectiveness in detecting BVID; C-scan did not produce promising results; shearography performed better, with the ability to indicate the extent of damage. Polimeno et al. [63] implemented nonlinear elastic wave spectroscopy to detect BVID in CF/EP composites, based on the shift in resonance frequency or the presence of harmonics and sidebands contained within the signals. Ross [64] and Zhang et al. [65] proposed piezoelectric sensor networks for real-time monitoring of structures to detect the location and time history of impact forces; these authors sought to detect impacts at the time they occurred and to locate them according to the time of arrival of impact vibrations at each sensor. Capineri et al. [66] used a network of flexible piezo-polymer transducers to detect artificial defects by calculating a damage index (DI) based on the difference in shape and amplitude of two signals from the same path in undamaged and damaged conditions. Takeda et al. [67] proposed a method based on changes in the amplitude ratio and the arrival time of Lamb waves to detect and assess delamination in CFRP laminates; the waves were generated by piezo-ceramic actuators and received by fiber Bragg grating (FBG) sensors. Later, Takeda et al. [68] demonstrated the ability of FBG sensors to perform long-term health monitoring of such large composite structures as an aircraft wing structure.

Recently, symbolic dynamics (SD) have been introduced to characterize time series responses in many applications including structural health monitoring (SHM) [69, 70], online fatigue damage monitoring using wave based signals [71], underwater object detection [72], anomaly detection in electronic systems [73], weather forecasting [74], and currency exchange monitoring [75]. In a structural system, SD evaluates the

52

progress of variation in the system dynamics to monitor any gradual change that indicates growing structural damage [76]. The application of this technique does not depend on the nature of the system, being deterministic or stochastic, linear or nonlinear [69, 70]. Rather, it centers on transforming time series records into symbol sequences, reducing computational time while conserving the main characteristics [69, 70]. Moreover, it has been demonstrated that this technique enhances the signal-to-noise ratio [77]. Minimum work has been done on the application of symbolic time series analysis (STSA) to ultrasonic waves; probably the only work reported in the literature was by Gupta et al. [71]. They made use of STSA for early detection and online monitoring of fatigue damage in polycrystalline alloys (7075-T6 aluminum) subjected to low-cycle and high-cycle fatigue. However, damage assessment using SD is becoming more recognized due to many successful applications in this field. In 2009, Rao et al. [78] published a comparative review to evaluate the efficiency of SD in detecting early damage compared to other methods such as principal component analysis, artificial neural networks, and kernel regression analysis. SD was demonstrated to be superior in early detection and computational efficiency. That study was based on time series determined from a nonlinear active electronic system. Li et al. [79] introduced a new method called symbolization-based differential evolution strategy (SDES) in which they integrated STSA with the differential evolution (DE) method for system identification in structural health monitoring. The authors performed both experimental and numerical analysis, in comparison with DE and particle swarm optimization, to verify the superiority of SDES even when dealing with relatively high noise contamination. Alamdari et al. [69, 70] proved the feasibility of STSA for the detection and localization of gradual deterioration in civil structures. Using numerical

53

simulations applied to a flexural beam and a 2-D planar truss bridge, they demonstrated the robustness of the method for different damage, excitation, and noise conditions. In other work, SD has been applied to detect anomalies in flexible mechanical couplings using simulated acceleration data sets [80] and anomalies in aircraft gas-turbine engines using time series extracted from the inputs and outputs of the numerically modeled dynamic system [81].

In this study, using ultrasonic guided waves, a robust scheme based on STSA is proposed to assess BVID in CF/EP sandwich composite structures. Damage was artificially introduced into a specimen by quasi-static indentation. Guided waves were excited and captured using piezoelectric wafers (PZTs). The anomaly rate, indicating the extent of damage in each path within the sensor network, was determined by STSA according to the maximum Shannon's entropy approach. As a result, an imaging algorithm was adopted to localize the damage based on the anomaly value obtained from each path. Further, progressive damage was also evaluated through correlation of various damage cases with their corresponding anomaly values.

## B. Experimental Setup

A sensor network consisting of 16 circular PZTs was surface-mounted on a plate. The PZT elements were distributed enclosing a square area as shown in Figure 28 (a), where the distance between neighboring PZT elements was 100 mm. The properties of the CF/EP sandwich panels are summarized in Table 10. During testing, one PZT element functioned as the actuator while the others functioned as sensors, and the role of the actuator alternated until all the PZT elements had functioned as the actuator. Sinusoidal tone bursts (90V peak-to-peak) enclosed in a Hanning window were used as

the input signal for the actuator. Activation and acquisition of wave signals were performed using an active signal generation and data acquisition system developed on the VXI platform, consisting mainly of a signal generator (Agilent© E1441), signal amplifier (PiezoSys® EPA-104), signal conditioner (Agilent© E3242A), and signal digitizer (Agilent© E1437A) (see Figure 29). The wave signals were captured at a sampling rate of 20.48 MHz. The acquisition duration was set to insure that the activated wave modes were captured, knowing the group velocities of individual wave modes.
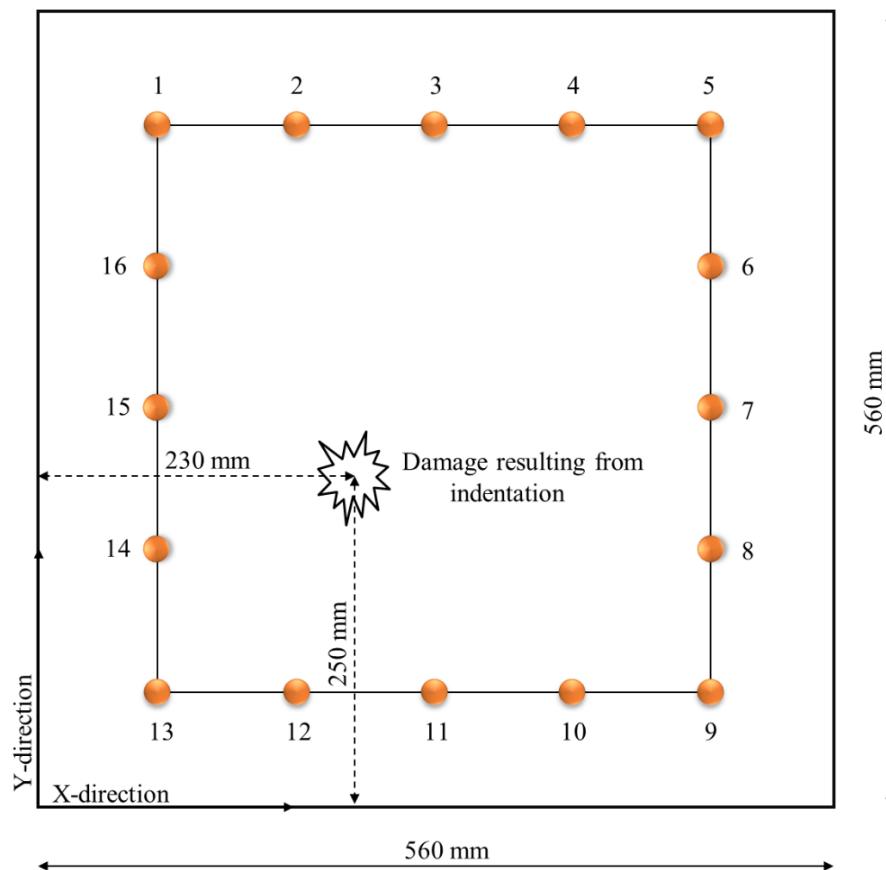


(a)
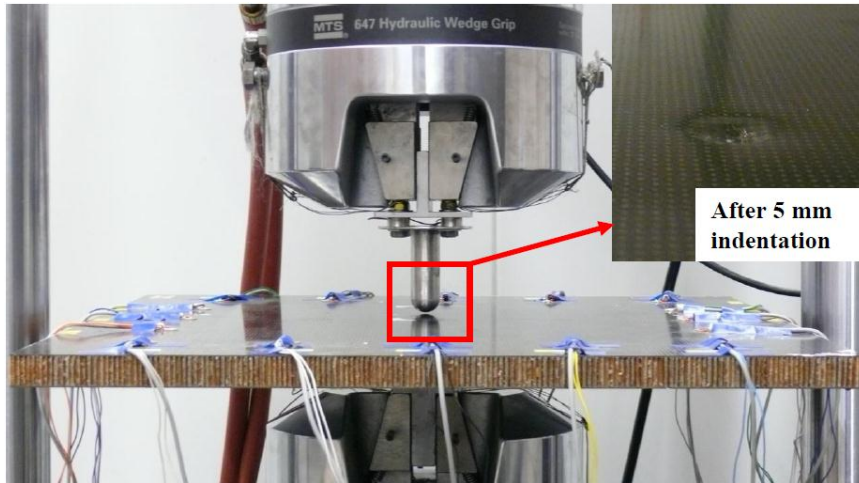
(b)

**Figure 28: CF/EP sandwich composite panel, (a) sensor network on the surface and (b) quasi-static loading and (inset) the resulting dent**
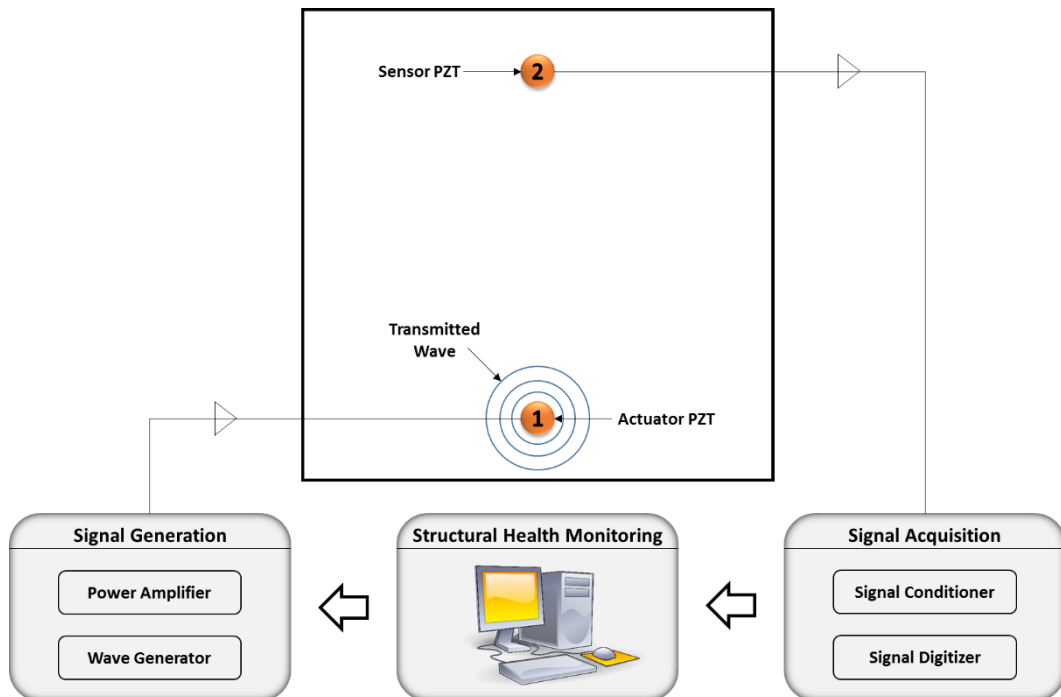


**Figure 29: Experimental setup**

The quasi-static indentation process was conducted on the sandwich composite panel using a steel indenter with a semi-spherical head set (Figure 28 (b)). Using the controlled displacement mode on a Materials Testing System (MTS), BVID was produced after 2, 3, and 5 mm indentations. The position of the indentation is shown in Figure 28 (a). After the indenter was removed, the skin was partially pushed back up, but a dent in the skin remained due to the damage that had occurred in the core (crushing) and the skin (e.g. fiber breakage, matrix cracking, delamination). After each indentation, the deformation on the plate surface, defined as the residual deformation, was measured using a dial indicator gauge. It was observed that the residual deformation depth increased with the increase in the indentation depth. The 2, 3, and 5 mm indentations resulted in peak residual deformations of 0.2, 0.5, and 2.7 mm respectively.

**Table 10: Properties of CF/EP sandwich panel**

(a) Properties of plain woven fabric CF/EP composite laminate

| $E_{11}$ | $E_{22}$ | $\nu_{12}$ | $G_{12}$ | $G_{23}$ | $G_{31}$ | $\nu_{13}$ | $\nu_{23}$ | Density |
|---|---|---|---|---|---|---|---|---|
| 55.8GPa | 55.8GPa | 0.06 | 3.65GPa | 3.65GPa | 3.65GPa | 0.05 | 0.38 | 1600 kg/m3 |

(b) Properties of Nomex core (HRH 10 1/8-4)

| Cell Diameter | Core Thickness | Density |
|---|---|---|
| 3.2 mm | 20.4 mm | 64 kg/m3 |

## C. Symbolic Time Series Analysis (STSA) for Guided Waves

### 1. Data Partitioning

Partitioning of a state space consists of the division of the space into a certain number of subsets called partitions. Those partitions should not have common information and, when assembled, they form the entire state space. That is, if $\{P_1, P_2, \ldots, P_S\}$ are the partitions of the state space $\Omega$, then both equations (1) and (2) are valid:

$$\bigcup_{i=1}^{S} P_i = \Omega \; \forall \; i \neq j \;\; ; \;\; i, j \in [1, S] \tag{1}$$

$$P_i \cap P_j = \emptyset \; \forall \; i \neq j \;\; ; \;\; i, j \in [1, S] \tag{2}$$

Time series data may be transformed into a symbol sequence by partitioning the state space into $S$ intervals, where each interval is represented by a symbol. After replacement of each value of the time series by the symbol of the partition to which it belongs, the symbol sequence of the time series can be established ([Figure 30](#)).

Shannon's entropy was used in order to specify an appropriate number of partitions and the corresponding thresholds $(\beta_i)$ (as shown in Figure 4). Shannon's entropy quantifies the amount of information. It is defined as:

$$H = -\sum_{k=1}^{k=S} p_k \log p_k \tag{3}$$

Where

- $p_k$: Probability of the $k^{\text{th}}$ symbol in the symbolic sequence

- $S$:  Number of symbols or number of partitions

Two important properties of Shannon's entropy worth highlighting are [69, 70]:

- <u>Property 1:</u> For a certain number of partitions $S$, the entropy $H$ is maximal if $p_i = p_j \; \forall \; i, j \in [1, S]$.

- **Property 2:** If $p_i = p_j \ \forall \ i, j \in [1, S]$, then as the number of partitions increases, the entropy $H$ increases.

These two features can be incorporated to select the optimal number of partitions and the suitable thresholds upon which the data is to be partitioned. When $p_i = p_j \ \forall \ i, j \in [1, S]$, then the probabilities of all symbols are equal, meaning that all the partitions contain the same number of data points. Therefore, according to "*Property 1*", the thresholds should be set to ensure that all the partitions contain the same number of data points.

Considering "*Property 2*", maximizing Shannon's entropy requires maximization of the number of partitions. The selection of a suitable number of partitions is critical. A large number of partitions leads to preservation of the noise contained in the signals and becomes computationally expensive. On the other hand, a small number of partitions can result in the loss of important information. On those bases, the significance of the entropy variation when increasing the number of partitions, while keeping those partitions equiprobable, was investigated. This variation value is defined in equation (4) and is known as the entropy excess:

$$Entropy \ excess = H(S + 1) - H(S) \tag{4}$$

while taking:

$$p_i = p_j \ \forall \ i, j \in [1, S] \Rightarrow p_k = \frac{1}{S} \ \forall \ k \in [1, S] \tag{5}$$

Figure 31 shows the variation of the entropy excess as a function of the number of partitions. It is observed that there is a sharp variation when considering a small number of partitions, while the variation approaches zero with the increase of the number of partitions. For $S \geq 9$, the variation in the entropy excess becomes less than

5%. Therefore, the choice of $S \geq 9$ is important for preserving the information content obtained from the original data.

A further consideration when choosing the number of partitions is the reduction ratio (R), which is defined as the ratio between the data size $N$ and the chosen number of partitions $S$:

$$R = N/S \qquad (6)$$

As R approaches 1, the original features of the signal are more conserved in the symbol sequence; noise is also conserved in case of noisy signals. In contrast, as $R$ increases above one, more features contained within the original signal are lost. As a consequence, the reduction ratio is a critical factor when choosing the number of partitions. In other words, if the number of partitions nears the data size, there will be a significant effect of small variations that may be noise due to operational and environmental effects. Therefore, the reduction ratio should be selected according to the desired resolution of the variation. Furthermore, the reduction ratio is the reduction in the computational power and time required for anomaly calculations. In fact, time reduction is one of the most important factors in an online structural health monitoring approach. With knowledge of this importance, the reduction ratio must be investigated according to our experimental results, and is discussed further in section 4 of this paper.

After selecting the number of partitions, suitable thresholds must be chosen. Those thresholds should ensure that the probabilities of occurrence of the symbols are equal in the healthy state (or in the benchmark data), i.e., all the partitions must contain the same number of data points. This maximizes Shannon's entropy and thus maximizes the amount of information preserved from the original data for this particular number of

partitions. When thresholds are set for the benchmark state of a specific path of the sensor network, they remain constant when dealing with other states of the same path.

Partitioning based on maximum entropy makes the intervals wider in regions with poor information content and narrower in information-rich regions. Figure 30 shows an example of a maximum entropy partitioning of one of the collected time series samples containing 220 data points ($N = 220$). The partitioned regions are labeled $P_1$ to $P_5$ ($S = 5$), where the dashed lines represent the threshold values ($\beta_1$, $\beta_2$, $\beta_3$, and $\beta_4$,).

Figure 32 illustrates the same sample of data as presented in Figure 30 after incrementally sorting the data points. As can be seen, the probabilities of the symbols are equal between different partitions. The vertical dotted lines are drawn to show the equal number of data points in each partition (each partition has strictly $220/5 = 44$ data points).
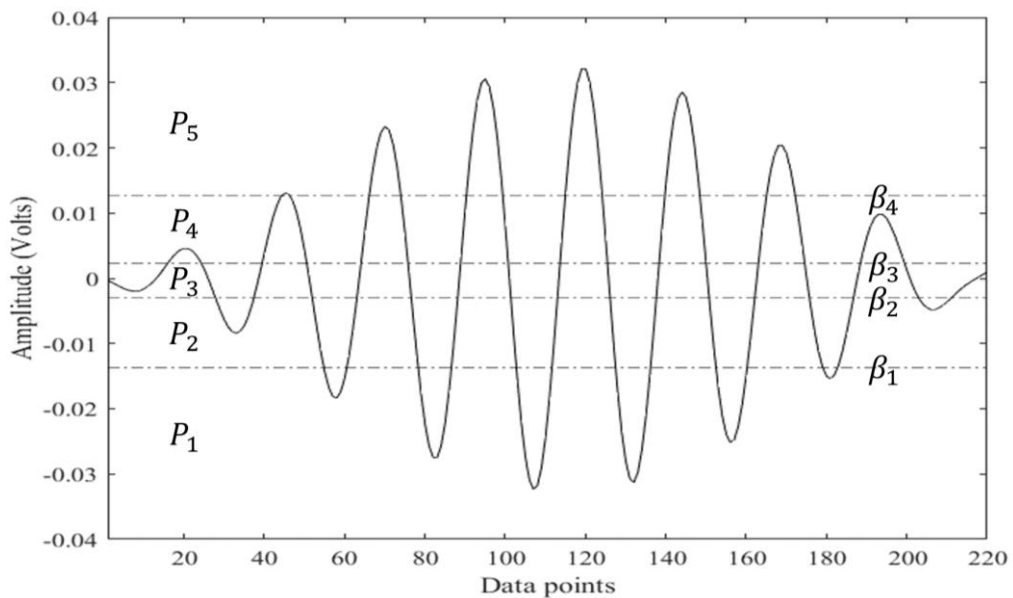


**Figure 30: Maximum entropy partitioning of raw time series data**
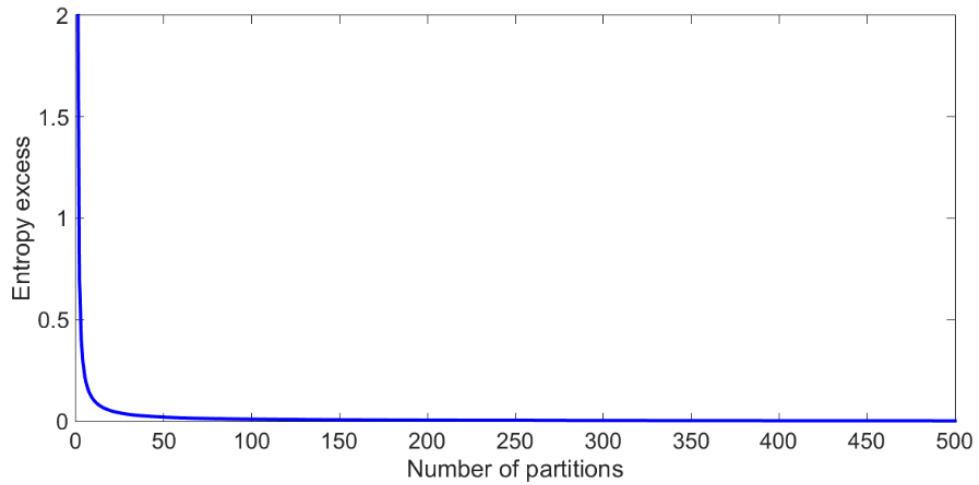
**Figure 31: The effect of number of partitions on the entropy excess.**
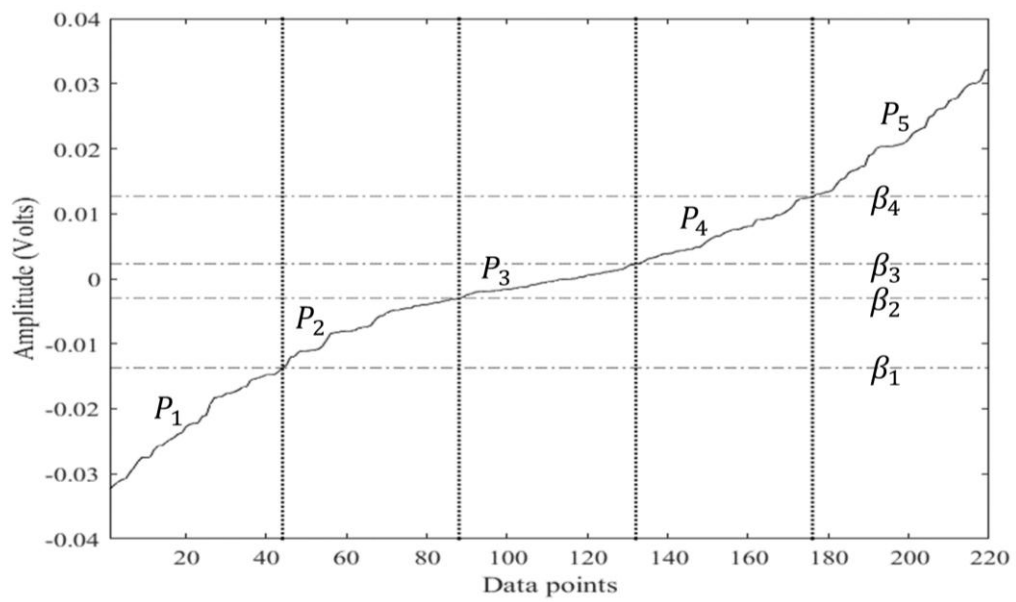


**Figure 32: Incrementally sorted time series data after partitioning to visualize equiprobable symbols.**

## 2. *Anomaly Detection Using SD*

Consider a dynamic system under testing at $T$ observation stages. A practical example might be a structure that is instrumented with a structural health monitoring system in which tests are performed regularly at spaced intervals or after a major incident. Each test yields $N$ data points at $M$ different sensing locations. The time series data obtained at an instant $t \in [1: T]$ and at a sensing location $m \in [1: M]$ can be represented as:

$$X_t^m = [x_1^m, x_2^m, \dots, x_N^m] \tag{7}$$

while the evolution of the system at location $m$ along the $T$ tests is represented by:

$$E^m = [X_1^m, X_2^m, \dots, X_T^m] \tag{8}$$

The first observation $X_1^m$ is considered the benchmark state for the location $m$. A distinct symbol space according to the maximum entropy approach can be constructed for each of the $m$ locations, separately (as discussed in section 3.1).

For every location, the symbol sequence $S_t^m$ can be generated by mapping the time data into the pre-constructed symbol space for that particular location. The probability of occurrence of each symbol in the sequence can be calculated and assembled into a probability vector, $V_t^m$. The anomaly measure $A_t^m$ is calculated according to the change in the magnitude of the probability vector compared to that of the benchmark state (equation (9)). The algorithm developed in this work includes the following steps:

- Select the number of partitions, $S$. Choose the same number of partitions for all the locations, to allow statistical comparison between different locations.

- From the first observation, determine the threshold values $\beta_i$ ; $i \in [1, S-1]$ according to the maximum entropy approach. This will create a symbol space for each of the $M$ locations.

- Determine the symbol sequence $S_t^m$ of the observation $X_t^m$.

- Determine the probability vector $V_t^m$. Notice that $V_1^m = \left[\frac{1}{S}, \frac{1}{S}, \ldots, \frac{1}{S}\right]$.

- Calculate $A_t^m$, the anomaly measure at location $m$ and at instant $t$ according to equation (9):

$$A_t^m = \left| 1 - \frac{\|V_t^m\|}{\|V_1^m\|} \right| \tag{9}$$

Where $\|V_1^m\|$ is the magnitude of the probability vector in the nominal state:

$$\|V_1^m\| = \sqrt{1/S} \tag{10}$$

## 3. *Localization of Damage and Data Fusion*

From the network of 16 PZT elements in the panel, 160 sensing paths are available. Due to the dual function of the PZT elements, the number of paths can be reduced to 80 distinct paths (e.g., instead of using both paths P1-P2 and P2-P1, only P1-P2 is considered). The anomaly measures obtained for these 80 paths (steps 1 to 5 in Section 3.2) are employed to construct a damage image (using data fusion technique). The damage location is expected to be located on the intersection of the most damaged paths, i.e. the paths having the highest anomaly measures.

After calculation of the anomaly measures of all 80 available paths, construction of the damage image is accomplished by dividing the monitored zone into uniform 1 mm$^2$ square-shaped grid points, where the existence of damage in each cell is

64

evaluated by merging the perceptions of the anomaly measures from all the sensing

paths. The damage index (DI) or the probability of damage at a cell (x, y) in the

observed zone is given by [82]:

$$DI(x, y) = \sum_{j=1}^{J} P_j (x, y) = \sum_{j=1}^{J} A_j f_j(z) \tag{11}$$

Where

• $P_j(x, y)$ is the probability of damage at cell (x, y) obtained from the anomaly

measure of the $j^{th}$ path.

• $A_j$ is the anomaly measure for the $j^{th}$ path.

• $f_j(z)$ is the normal distribution function for the $j^{th}$ path (defined below).

To account for the possible existence of damage near the paths, the influence of

the anomaly measure is considered in the shape of a normal distribution function having

a maximum effect on the path and decreasing away from it. This normal distribution

function is defined by:

$$f(z) = \frac{1}{\sigma\sqrt{2\pi}} e^{\frac{-(z-\mu)^2}{2\sigma^2}} \quad for \quad -\infty < z < +\infty \tag{12}$$

Where

• $\mu$ is the mean of the normal distribution model.

• $\sigma$ is the standard deviation of the normal distribution model.

According to our experimental investigations for the used sandwich structure, $\mu$

and $\sigma$ were fixed at 0 and 40 mm respectively. Further, $z$ was determined by assigning

the same effect of damage for all the grid points that were equidistant from the path.

This was conducted by considering a rectangular affected zone for each sensing path

during the fusion process where $z$ was defined as [82]:

$$z = \frac{d}{D_j} \tag{13}$$

Where

- $d$ is the normal distance separating the grid point from the $j^{th}$ sensing path.

- $D_j$ is the distance separating the actuator and the sensor of the $j^{th}$ path.

A flowchart summarizing the main steps of the damage identification algorithm presented in this paper is shown in Figure 33.
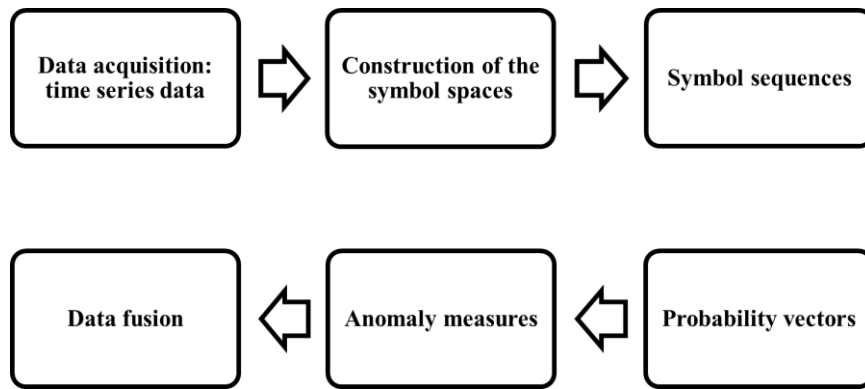


**Figure 33: Damage localization flowchart.**

## D. Results and Discussion

The number of partitions was set at $S = 20$ (the reason for the selection of $S = 20$ is discussed further below) and the STSA method with maximum entropy partitioning was applied on the collected data of $N = 220$ data points. After computation of the anomaly measures, damage images were constructed as explained in section 3.3. Figures 34 (a), 34 (b), and 34 (c) respectively show the constructed images of three damage cases after 2, 3, and 5 mm of indentation when the excitation frequency of 250 KHz was used. As clearly seen, damage was reliably identified in all three test cases, even in the case of the smallest surface dent (order of 0.2 mm) that occurred after the 2 mm indentation. The localization method appeared to be very effective in Figure

66

34 (b) when considering a dent 0.5 mm in depth (after 3 mm indentation). Moreover, after the 5 mm indentation, and with a dent depth of 2.7 mm, the localization of damage is demonstrated to be very precise, as shown in Figure 34 (c) (less than 13 mm distance between actual and predicted location). However, uncertainty as to location is evident for the 0.2 mm dent, which is considered to be very small (Figure 34 (a)).

Different excitation frequencies of 150, 175, 200, and 250 KHz were used to investigate the state of the sandwich structure. The distances between the actual and the predicted locations of the damage are summarized in Table 11. $\Delta x$ and $\Delta y$ are, respectively, the distances between the actual and the predicted damage locations in the *x* and *y* directions (a coordinates system was defined in Figure 29 (a)).

The distance between the actual and the predicted location of the dent after 5 mm indentation was less than 26 mm for all excitation frequencies. Nevertheless, excitation frequencies ranging between 175 KHz and 250 KHz for the 3 mm indentation damage led to accurate predictions of the dent location within a distance of less than 55 mm (from the actual location). However, the prediction of the damage location for the 2 mm indentation damage was less accurate; the best result, that was within 70 mm of the actual location, was observed at an excitation frequency of 250 KHz,

**Table 11: Distances between actual and predicted damage locations using different excitation frequencies and based on 20 partitions.**

| Partitions | 20 | | | | | | | | |
|---|---|---|---|---|---|---|---|---|---|
| Indentation depth (mm) | 2 | | | 3 | | | 5 | | |
| Frequency (KHz) | $\Delta x$ (mm) | $\Delta y$ (mm) | Distance (mm) | $\Delta x$ (mm) | $\Delta y$ (mm) | Distance (mm) | $\Delta x$ (mm) | $\Delta y$ (mm) | Distance (mm) |
| 150 | 59.00 | 188.00 | 197.04 | 70.00 | 178.00 | 191.27 | 25.00 | 2.00 | 25.08 |
| 175 | 79.00 | 102.00 | 129.02 | 46.00 | 27.00 | 53.34 | 13.00 | 0.00 | 13.00 |
| 200 | 75.00 | 35.00 | 82.76 | 33.00 | 43.00 | 54.20 | 10.00 | 5.00 | 11.18 |
| 250 | 7.00 | 67.00 | 67.36 | 11.00 | 27.00 | 29.15 | 8.00 | 9.00 | 12.04 |
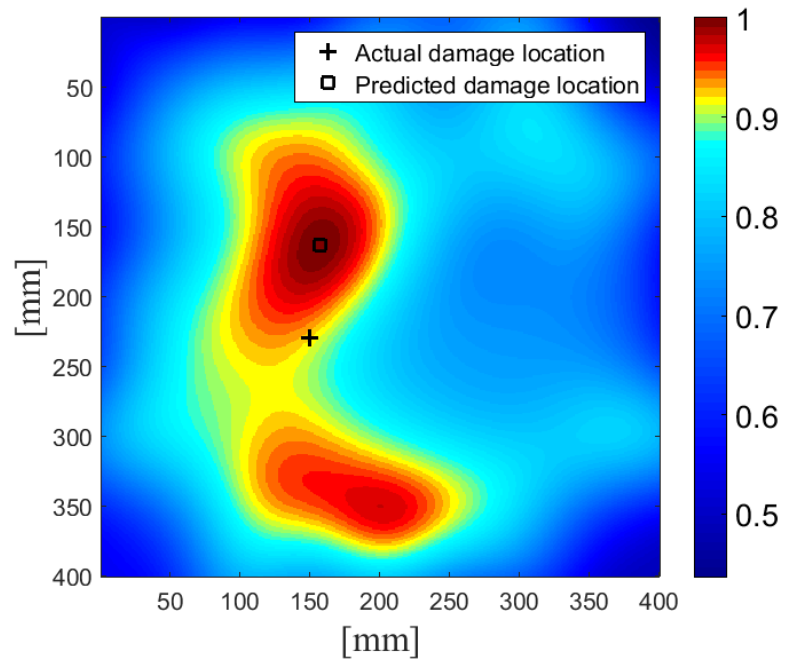
(a)
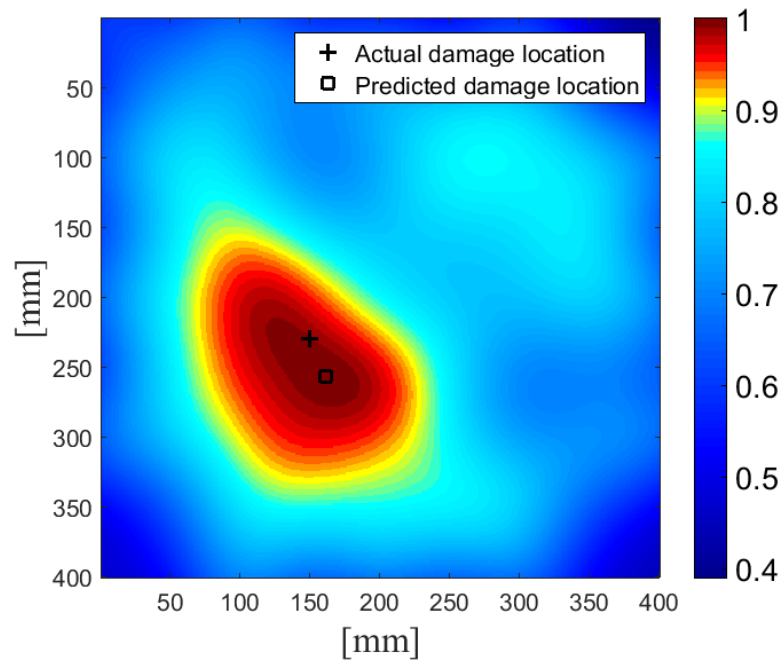
(b)
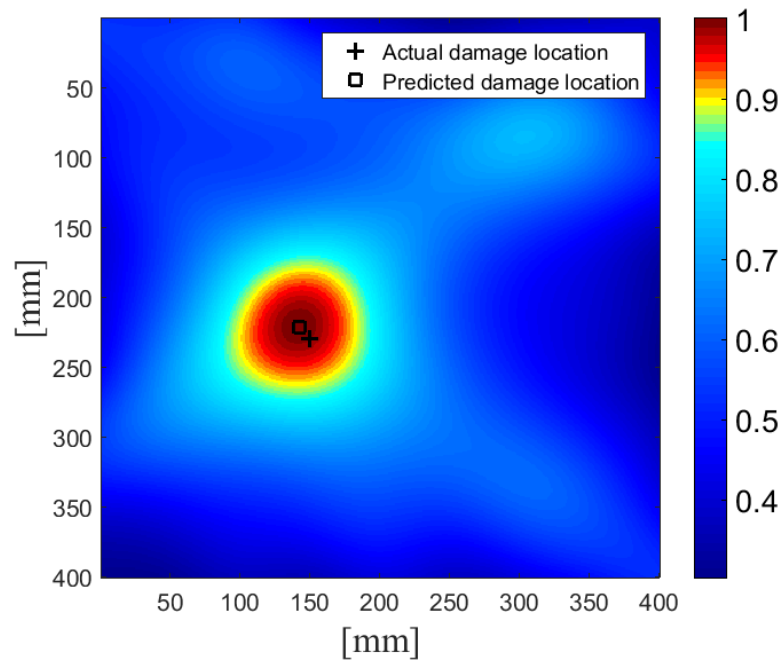


(c)

**Figure 34: Reconstructed images for indentation damage using 250 KHz excitation frequency and based on 20 partitions: (a) 2 mm, (b) 3 mm, and (c) 5 mm indentation depth.**

69

The effects of the number of partitions on the damage prediction and on computational time were also investigated, considering only the two excitation frequencies of 200 and 250 KHz. The analysis was performed for each of the above selected frequencies, applying different numbers of partitions using all the possible divisors of 220, that was the data set size. The results are summarized in Tables 12 and 13; it is evident that an increase in the number of partitions improves the localization accuracy to a certain limit, after which it begins to drop. The reduction in the precision for higher numbers of partitions $S$ may be due to the increased sensitivity to small variations and the significant influence of noise when the value of $S$ is closer to the size of the data set. When $S = 220$ partitions, that is, is equal to the data set size, this means each data point in the benchmark data set is considered as a partition ($i.e.\, R = 1$), and this is where the greatest noise effect is obtained because any small variation from the benchmark data points in the new captured measurements can be considered an anomaly. In contrast, when $S$ decreases ($i.e.,\, R$ increases), there is loss of information and consequently lower precision; this may explain the significant increase in the error for the smallest value of $S$ considered in this study ($S = 2\, \&\, R = 110$).

The results given in Tables 12 and 13 showed that the number of partitions could vary from 10 to 22 while maintaining adequate precision (also $10 \leq R \leq 22$).

**Table 12: Distances between actual and predicted damage locations at 200 KHz excitation frequency for different numbers of partitions.**

| Frequency (KHz) | 200 kHz | | | | | | | | |
|---|---|---|---|---|---|---|---|---|---|
| Indentation Depth (mm) | 2 | | | 3 | | | 5 | | |
| Partitions | Δx (mm) | Δy (mm) | Distance (mm) | Δx (mm) | Δy (mm) | Distance (mm) | Δx (mm) | Δy (mm) | Distance (mm) |
| 2 | 29.00 | 127.00 | 130.27 | 50.00 | 28.00 | 57.31 | 62.00 | 162.00 | 173.46 |
| 4 | 85.00 | 25.00 | 88.60 | 62.00 | 15.00 | 63.79 | 30.00 | 5.00 | 30.41 |
| 5 | 79.00 | 31.00 | 84.86 | 35.00 | 42.00 | 54.67 | 15.00 | 19.00 | 24.21 |
| 10 | 85.00 | 22.00 | 87.80 | 34.00 | 44.00 | 55.61 | 12.00 | 8.00 | 14.42 |
| 11 | 58.00 | 63.00 | 85.63 | 39.00 | 37.00 | 53.76 | 14.00 | 7.00 | 15.65 |
| 20 | 75.00 | 35.00 | 82.76 | 33.00 | 43.00 | 54.20 | 10.00 | 5.00 | 11.18 |
| 22 | 67.00 | 41.00 | 78.55 | 41.00 | 32.00 | 52.01 | 13.00 | 9.00 | 15.81 |
| 44 | 24.00 | 117.00 | 119.44 | 47.00 | 25.00 | 53.24 | 16.00 | 13.00 | 20.62 |
| 55 | 66.00 | 40.00 | 77.18 | 49.00 | 25.00 | 55.01 | 21.00 | 13.00 | 24.70 |
| 110 | 6.00 | 144.00 | 144.12 | 65.00 | 7.00 | 65.38 | 30.00 | 7.00 | 30.81 |
| 220 | 32.00 | 155.00 | 158.27 | 69.00 | 8.00 | 69.46 | 48.00 | 6.00 | 48.37 |

**Table 13: Distances between actual and predicted damage locations at 250 KHz excitation frequency for different numbers of partitions.**

| Frequency (KHz) | 250 kHz | | | | | | | | |
|---|---|---|---|---|---|---|---|---|---|
| Indentation Depth (mm) | 2 | | | 3 | | | 5 | | |
| Partitions | Δx (mm) | Δy (mm) | Error Distance (mm) | Δx (mm) | Δy (mm) | Error Distance (mm) | Δx (mm) | Δy (mm) | Error Distance (mm) |
| 2 | 23.00 | 61.00 | 65.19 | 62.00 | 159.00 | 170.66 | 144.00 | 154.00 | 210.84 |
| 4 | 27.00 | 70.00 | 75.03 | 22.00 | 24.00 | 32.56 | 149.00 | 153.00 | 213.56 |
| 5 | 99.00 | 11.00 | 99.61 | 21.00 | 14.00 | 25.24 | 6.00 | 14.00 | 15.23 |
| 10 | 12.00 | 22.00 | 25.06 | 7.00 | 10.00 | 12.21 | 3.00 | 12.00 | 12.37 |
| 11 | 62.00 | 104.00 | 121.08 | 6.00 | 12.00 | 13.42 | 4.00 | 13.00 | 13.60 |
| 20 | 7.00 | 67.00 | 67.36 | 11.00 | 27.00 | 29.15 | 8.00 | 9.00 | 12.04 |
| 22 | 72.00 | 20.00 | 74.73 | 17.00 | 27.00 | 31.91 | 10.00 | 12.00 | 15.62 |
| 44 | 53.00 | 112.00 | 123.91 | 33.00 | 30.00 | 44.60 | 10.00 | 11.00 | 14.87 |
| 55 | 10.00 | 100.00 | 100.50 | 38.00 | 17.00 | 41.63 | 11.00 | 9.00 | 14.21 |
| 110 | 64.00 | 23.00 | 68.01 | 63.00 | 30.00 | 69.78 | 12.00 | 12.00 | 16.97 |
| 220 | 68.00 | 28.00 | 73.54 | 71.00 | 32.00 | 77.88 | 22.00 | 5.00 | 22.56 |

As for computational time, both frequencies resulted in approximately the same values for different numbers of partitions, meaning that the elapsed time was not affected by excitation frequency. Figure 35 shows the influence of changing the number of partitions on the computational time for calculating the anomaly values for all

existing paths within the sensor network. It is evident that the computational time is linearly proportional to the number of partitions. As the reduction ratio increases ($S$ decreases), the time needed for anomaly calculations decreases at the same rate, demonstrating an advantage of using STSA, that demands less computational time than other approaches that do not contain any means of data reduction. For instance, using $S = 20$ partitions, the best precision for damage localization was obtained while reducing the computational time by approximately the same value of the reduction ratio ($R = 11$), and the time elapsed to calculate anomaly values was less than 0.5 sec. In this case, dimensionality reduction made this approach suitable for online structural health monitoring and instantaneous damage localization and assessment.
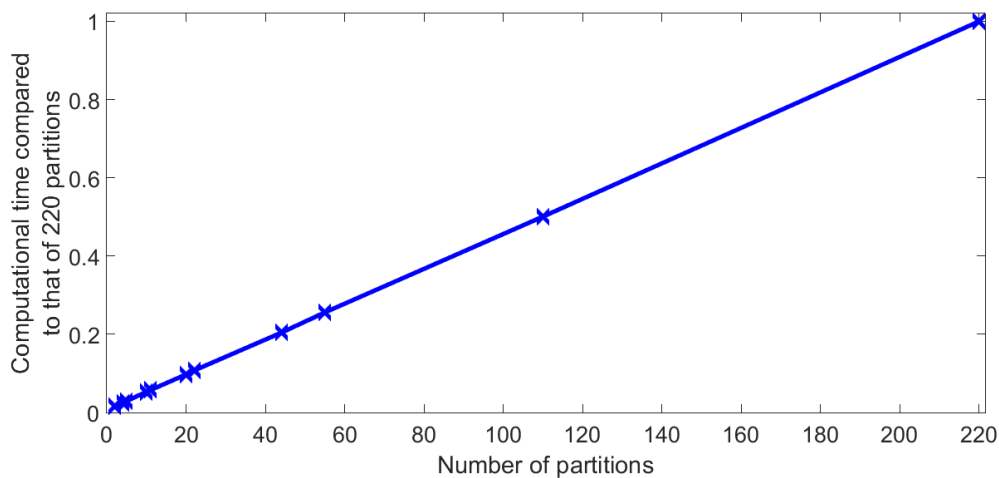


**Figure 35: Computational time for calculating anomaly values of all existing paths versus the number of partitions.**

The capability of the approach to evaluate the severity of damage was also investigated. Figure 36 shows the mean values of the anomaly measures obtained from all the existing paths for the three damage sizes (2, 3, and 5 mm indentation). It can be

72

observed that when the size of damage increases, the mean anomaly value also

increases, indicating that the severity of damage may be deduced or at least predicted

from the obtained anomaly values. Comparison between damage sizes is obviously

possible from the results obtained, and there appears to be an approximately linear

relationship between the size of damage and the average anomaly value of all paths. To

predict the damage size, training of the system on different damage sizes would be

required.
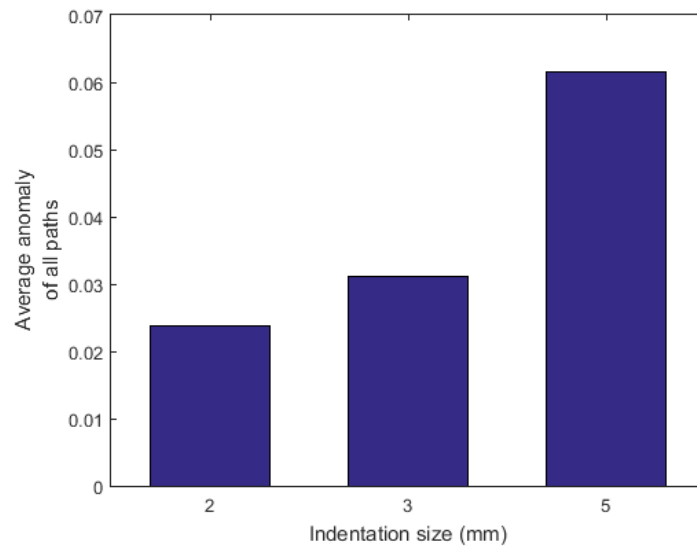


**Figure 36: Mean values of the anomaly measures obtained from the existing 80 paths using an excitation frequency of 250 KHz and 20 partitions.**

# CHAPTER IV

# CONCLUSION

This work presented different methods of signal processing and feature extraction of time series based on ultrasonic guided wave responses. Lamb waves of various frequencies were excited for the study of their proficiency in damage detection and assessment in composite and metallic structures as well. The studied defects were worm holes found in friction-stir-welded AZ31B magnesium alloy plates of 3 mm thickness, and BVID in a CF/EP composite-sandwich-structured specimen. The approaches were applied on the fundamental symmetric ($S_0$) mode for its known sensitivity to small variations in structures.

In the first study, the capability of Lamb waves of qualifying FSW in AZ31B magnesium alloy was demonstrated. Different weld qualities were obtained in four different FSW plates through changing a welding parameter. Waves were induced and received by PZT wafers attached to the surfaces of the plates on both sides of the weld. Four frequencies were chosen for investigations, and a DI was proposed based on the amplitude variation from the response of a non-welded plate. The complexity of the responses due to reflections and superpositions was solved by a powerful separation technique called "improved CEEMDAN". CT-scanning was used as an NDT to classify the plates according to their actual weld qualities, and the CT-images were used to build 3D models of the plates using "Mimics" software. FE simulations were then performed on the 3D models using "Abaqus" and the numerical responses were subjected to the same processing approach. The DIs computed from experimental results showed a good match to the weld qualities with some minor errors that may be due to noise, while the

DIs computed from FEA were all giving the correct classification of the welds for the 4 used excitation frequencies. According to the results, the use of 200, 300, 400, and 500KHz as working frequencies for such an application is recommended, but the most precise results are expected when using a 300 KHz frequency. After that, damage volumes were determined from the 3D models in a region of about 30.5 mm around the sensing path using "Mimics". The volumes were then used to propose an equation between the damage volume and the DI calculated from the responses of the 300KHz frequency wave. This relation was then applied on a case study of a new FSW AA7020-T651 aluminum alloy plate to predict the damage volume. The prediction error was less than 12% from the damage volume determined using "Mimics" from the plate's CT-scan. This relation will be the subject of more in-depth investigations in the future, and a training technique may be needed for a more efficient prediction.

In the second study, detection, localization, and evaluation of progressively increasing BVID in a sandwich CF/EP composite structure was investigated using symbolic time series analysis (STSA). The analysis was applied on ultrasonic guided wave signals actuated and sensed using a PZT network installed on a sample plate. Partitioning of the original data was performed based on maximizing the Shannon's entropy, to retain maximum information content from the original signal while eliminating noise effects. An anomaly in a sensor path was defined as the ratio between the norms of probability vectors obtained from the constructed symbol sequences before and after damage had occurred, and the damage index (DI) of each 1 mm$^2$ square-shaped cell of the plate was obtained by data fusion combining information from all existing paths. Finally, an imaging algorithm was implemented to construct the images of the predicted damages. The effects of the excitation frequency and the number of

partitions on the resolution of the prediction were investigated. Best results were obtained at an excitation frequency of 250 KHz and after partitioning the data into 1/11 of its original size. The approach proved to be very sensitive to the existence of the smallest damage in the order of 0.2 mm after 2 mm indentation. This method was also able to locate the damage position precisely for indentation damage of 0.5 and 2.7 mm. Furthermore, the anomaly values determined in the approach were a good indicator of the increasing damage size. In addition, the computational time elapsed for calculating the anomaly values of all the investigated paths was shown to be very low (order of hundreds of milliseconds). These characteristics make the approach highly promising for online health monitoring of structures and for damage assessment and damage localization in real life applications. A drawback of the approach is the need for a large number of sensors to be placed to achieve the capability of damage localization. This can make the real life implementation more complex. Further optimization is therefore required to obtain the optimal number and locations of the sensors. Future work may also include improvement for better localization of very small damage sizes and testing the capability of the approach to detect and localize multiple defects.

As a conclusion, Lamb waves are highly sensitive to defects in both metallic and composite materials, and the suggested methodologies may be used for assessment in various applications, such as FSW process optimization, global NDT of new-born or in-use parts, and for structural health monitoring (SHM) with the potential of data reduction and minimization of computational time and power.

# REFERENCES

1. Ostachowicz, W., et al., *Guided Waves in Structures for SHM : The Time - domain Spectral Element Method*. Vol. 1. 2011, Hoboken: Wiley.

2. Rytter, A., *Vibration based inspection of Civil Engineering Structures PhD Thesis Aalborg University Denmark*. 1993.

3. Worden, K. and J. Dulieu-Barton, *An overview of intelligent fault detection in systems and structures*. Structural Health Monitoring, 2004. **3**(1): p. 85-98.

4. Delsanto, P.P., *Universality of nonclassical nonlinearity*. 2006: Springer.

5. Su, Z., L. Ye, and Y. Lu, *Guided Lamb waves for identification of damage in composite structures: A review*. Journal of Sound and Vibration, 2006. **295**(3): p. 753-780.

6. Mustapha, S. and L. Ye, *Propagation behaviour of guided waves in tapered sandwich structures and debonding identification using time reversal*. WAVE MOTION, 2015. **57**: p. 154-170.

7. Mustapha, S., et al., *Evaluation of barely visible indentation damage (BVID) in CF/EP sandwich composites using guided wave signals*. Mechanical Systems and Signal Processing, 2016. **76-77**: p. 497-517.

8. Badcock, R.A. and E.A. Birt, *The use of 0-3 piezocomposite embedded Lamb wave sensors for detection of damage in advanced fibre composites*. Smart Materials and Structures, 2000. **9**: p. 291.

9. Michaels, J.E. and T.E. Michaels, *Guided wave signal processing and image fusion for in situ damage localization in plates*. Wave Motion, 2007. **44**(6): p. 482-492.

10. Rathod, V.T. and D. Roy Mahapatra, *Ultrasonic Lamb wave based monitoring of corrosion type of damage in plate using a circular array of piezoelectric transducers*. NDT and E International, 2011. **44**(7): p. 628-636.

11. Mustapha, S., et al., *Debonding detection in composite sandwich structures based on guided waves*. AIAA journal, 2012. **50**(8): p. 1697-1706.

12. Bagheri, A., K. Li, and P. Rizzo, *Reference-free damage detection by means of wavelet transform and empirical mode decomposition applied to Lamb waves*. Journal of Intelligent Material Systems and Structures, 2013. **24**(2): p. 194-208.

13. Mustapha, S. and L. Ye, *Damage Identification and Assessment in Tapered Sandwich Structures Using Guided Waves*. Key Engineering Materials, 2013. **558**: p. 25-38.

14. Mustapha, S. and L. Ye, *Leaky and non-leaky behaviours of guided waves in CF/EP sandwich structures*. Wave Motion, 2014. **51**(6): p. 905-918.

15. Ge, L., X. Wang, and C. Jin, *Numerical modeling of PZT-induced Lamb wave-based crack detection in plate-like structures*. Wave Motion, 2014. **51**(6): p. 867-885.

16. Su, Z. and L. Ye, *Lamb wave-based quantitative identification of delamination in CF/EP composite structures using artificial neural algorithm*. Composite Structures, 2004. **66**(1): p. 627-637.

17. Cuc, A., et al., *Structural health monitoring with piezoelectric wafer active sensors for space applications*. AIAA journal, 2007. **45**(12): p. 2838-2850.

18.    Valle, C. and J.W. Littles, *Flaw localization using the reassigned spectrogram on laser-generated and detected Lamb modes.* Ultrasonics, 2002. **39**(8): p. 535-542.

19.    Anton, S.R., D.J. Inman, and G. Park, *Reference-free damage detection using instantaneous baseline measurements.* AIAA journal, 2009. **47**(8): p. 1952-1964.

20.    Mustapha, S., et al., *Assessment of debonding in sandwich CF/EP composite beams using A 0 Lamb wave at low frequency.* Composite structures, 2011. **93**(2): p. 483-491.

21.    Babu, A.S. and C. Devanathan, *An Overview of Friction Stir Welding.* Int. J. Res. Mech. Eng. Technol, 2013. **3**(2): p. 259-265.

22.    Thomas, W., et al., *Friction stir welding.* International patent application no. PCT/GB92102203 and Great Britain patent application, 1991(9125978.8).

23.    Thomas, W., et al., *Improvements relating to friction welding.* Patent NumberEP 0653265, 1995.

24.    Muthukrishnan, M. and K. Marimuthu. *Some studies on mechanical properties of friction stir butt welded Al-6082-T6 plates.* in *Frontiers in Automobile and Mechanical Engineering (FAME), 2010.* 2010. IEEE.

25.    Zhao, Y.-h., et al., *The influence of pin geometry on bonding and mechanical properties in friction stir weld 2014 Al alloy.* Materials Letters, 2005. **59**(23): p. 2948-2952.

26.    Kumbhar, N. and K. Bhanumurthy, *Friction stir welding of Al 6061 alloy.* Asian J. Exp. Sci, 2008. **22**(2): p. 63-74.

27.    Kumar, H.A. and V.V. Ramana, *An Overview of Friction Stir Welding (FSW): A New Perspective.* Research Inventy: International Journal of Engineering And Science, 2014. **4**(6): p. 01-04.

28.    Ammouri, A., et al. *FEM optimization of process parameters and in-process cooling in the friction stir processing of magnesium alloy AZ31B.* in *ASME 2013 International Mechanical Engineering Congress and Exposition.* 2013. American Society of Mechanical Engineers.

29.    Ammouri, A. and R. Hamade, *On the selection of constitutive equation for modeling the friction stir processes of twin roll cast wrought AZ31B.* Materials & Design, 2014. **57**: p. 673-688.

30.    Ammouri, A.H. and R.F. Hamade. *Comparison of Material Flow Stress Models toward More Realistic Simulations of Friction Stir Processes of Mg AZ31B.* in *Advanced Materials Research.* 2014. Trans Tech Publ.

31.    Ammouri, A.H., A.H. Kheireddine, and R.F. Hamade. *A Numerical Model for Predicting the Zener-Hollomon Parameter in the Friction Stir Processing of AZ31B.* in *Materials Science Forum.* 2014. Trans Tech Publications.

32.    Kheireddine, A., et al. *Experimentally Validated Thermo-Mechanically Coupled FE Simulations of Al/Mg Friction Stir Welded Joints.* in *ASME 2013 International Mechanical Engineering Congress and Exposition.* 2013. American Society of Mechanical Engineers.

33.    El Chlouk, Z., et al. *Intermetallic Compound Formation in Al/Mg Friction Stir Welded (FSW) Butt Joints.* in *ASME 2014 International Mechanical Engineering Congress and Exposition.* 2014. American Society of Mechanical Engineers.

34.    Mishra, R.S. and Z. Ma, *Friction stir welding and processing.* Materials Science and Engineering: R: Reports, 2005. **50**(1): p. 1-78.

35.    Threadgill, P. and A. Leonard, *Macro and microstructural features of friction stir welds in various materials.* TWI Rept, 1999.

36. Arbegast, W.J., *Friction Stir Joining: Characteristic Defects.* South Dakota School of Mines and Technology, 2003.

37. Nandan, R., T. DebRoy, and H. Bhadeshia, *Recent advances in friction-stir welding–process, weldment structure and properties.* Progress in Materials Science, 2008. **53**(6): p. 980-1023.

38. Burch, S. and N. Bealing, *A physical approach to the automated ultrasonic characterization of buried weld defects in ferritic steel.* NDT international, 1986. **19**(3): p. 145-153.

39. Karim, M., M. Awal, and T. Kundu, *Elastic wave scattering by cracks and inclusions in plates: in-plane case.* International Journal of Solids and Structures, 1992. **29**(19): p. 2355-2367.

40. Alleyne, D.N. and P. Cawley, *Optimization of Lamb wave inspection techniques.* Ndt & E International, 1992. **25**(1): p. 11-22.

41. Dixon, S., C. Edwards, and S.B. Palmer, *A laser-EMAT system for ultrasonic weld inspection.* ULTRASONICS, 1999. **37**(4): p. 273-281.

42. Cawley, P., et al., *Practical long range guided wave inspection-applications to pipes and rail.* Materials evaluation, 2003. **61**(1): p. 66-74.

43. Kažys, R., et al., *3D Analysis of interaction of Lamb waves with defects in loaded steel plates.* Ultrasonics, 2006. **44**: p. e1127-e1130.

44. Arone, M., D. Cerniglia, and V. Nigrelli, *Defect characterization in Al welded joints by non-contact Lamb wave technique.* Journal of Materials Processing Technology, 2006. **176**(1): p. 95-101.

45. Lu, M., et al. *Guided-wave-based detections of weld and crack in steel plates.* in *Second International Conference on Smart Materials and Nanotechnology in Engineering.* 2009. International Society for Optics and Photonics.

46. Martín, Ó., et al., *Assessment of resistance spot welding quality based on ultrasonic testing and tree-based techniques.* Journal of Materials Processing Technology, 2014. **214**(11): p. 2478-2487.

47. Liu, J., et al., *Ultrasonic test of resistance spot welds based on wavelet package analysis.* Ultrasonics, 2015. **56**: p. 557-565.

48. Santos, J. and M. Santos, *Lamb waves technique applied to the characterization of defects in friction stir welding of aluminum plates: comparison with X-ray and ultrasonic C-scan.* Journal of Testing and Evaluation, 2010. **38**(5): p. 1-6.

49. Delrue, S., et al., *Applying a nonlinear, pitch-catch, ultrasonic technique for the detection of kissing bonds in friction stir welds.* Ultrasonics, 2016. **68**: p. 71-79.

50. Tabatabaeipour, M., et al., *Non-destructive ultrasonic examination of root defects in friction stir welded butt-joints.* NDT & E International, 2016. **80**: p. 23-34.

51. Nguyen, Q. and M. Gupta, *Increasing significantly the failure strain and work of fracture of solidification processed AZ31B using nano-Al 2 O 3 particulates.* Journal of Alloys and Compounds, 2008. **459**(1): p. 244-250.

52. Palaniswamy, H., G. Ngaile, and T. Altan, *Finite element simulation of magnesium alloy sheet forming at elevated temperatures.* Journal of Materials Processing Technology, 2004. **146**(1): p. 52-60.

53. Huang, N.E., et al. *The empirical mode decomposition and the Hilbert spectrum for nonlinear and non-stationary time series analysis.* in *Proceedings of the Royal Society of London A: Mathematical, Physical and Engineering Sciences.* 1998. The Royal Society.

54. Wu, Z. and N.E. Huang, *Ensemble empirical mode decomposition: a noise-assisted data analysis method.* Advances in adaptive data analysis, 2009. **1**(01): p. 1-41.

55. Yeh, J.-R., J.-S. Shieh, and N.E. Huang, *Complementary ensemble empirical mode decomposition: A novel noise enhanced data analysis method.* Advances in Adaptive Data Analysis, 2010. **2**(02): p. 135-156.

56. Torres, M.E., et al. *A complete ensemble empirical mode decomposition with adaptive noise.* in *Acoustics, speech and signal processing (ICASSP), 2011 IEEE international conference on.* 2011. IEEE.

57. Colominas, M.A., G. Schlotthauer, and M.E. Torres, *Improved complete ensemble EMD: A suitable tool for biomedical signal processing.* Biomedical Signal Processing and Control, 2014. **14**: p. 19-29.

58. Meo, M., R. Vignjevic, and G. Marengo, *The response of honeycomb sandwich panels under low-velocity impact loading.* International Journal of Mechanical Sciences, 2005. **47**(9): p. 1301-1325.

59. DeFrancisci, G., et al., *Impact Damage Formation on Composite Aircraft Structures.*

60. Becz, S., J. Hurtado, and I. Lapczyk. *Analysis of barely visible impact damage for aerospace structures.* in *16th International conference on composite materials, Kyoto, Japan.* 2007.

61. Staszewski, W., S. Mahzan, and R. Traynor, *Health monitoring of aerospace composite structures–Active and passive approach.* Composites Science and Technology, 2009. **69**(11): p. 1678-1685.

62. Růžek, R., R. Lohonka, and J. Jironč, *Ultrasonic C-Scan and shearography NDI techniques evaluation of impact defects identification.* NDT and E International, 2006. **39**(2): p. 132-142.

63. Polimeno, U. and M. Meo, *Detecting barely visible impact damage detection on aircraft composites structures.* Composite Structures, 2009. **91**(4): p. 398-402.

64. Ross, R.W. *Structural health monitoring and impact detection using neural networks for damage characterization.* in *Proceedings of the 47th AIAA/ASME/ASCE/AHS/ASC Structures, Structural Dynamics, and Materials Conference.* 2006.

65. Zhang, D.C., et al. *A novel real-time health monitoring system for unmanned vehicles.* in *SPIE Defense and Security Symposium.* 2008. International Society for Optics and Photonics.

66. Capineri, L., et al., *Lamb Wave Ultrasonic System for Active Mode Damage Detection in Composite Materials.* Chemical Engineering Transactions, 2013. **33**: p. 577-582.

67. Takeda, N., et al., *Development of smart composite structures with small-diameter fiber Bragg grating sensors for damage detection: Quantitative evaluation of delamination length in CFRP laminates using Lamb wave sensing.* Composites Science and Technology, 2005. **65**(15): p. 2575-2587.

68. Takeda, N., et al., *Structural health monitoring of composite wing structure during durability test.* Composite Structures, 2007. **79**(1): p. 133-139.

69. Alamdari, M.M., J. Li, and B. Samali, *Damage Localisation Using Symbolic Time Series Approach*, in *Dynamics of Civil Structures, Volume 4.* 2014, Springer. p. 109-115.

70. Makki Alamdari, M., B. Samali, and J. Li, *Damage localization based on symbolic time series analysis.* Structural Control and Health Monitoring, 2015. **22**(2): p. 374-393.

71. Gupta, S., A. Ray, and E. Keller, *Online fatigue damage monitoring by ultrasonic measurements: A symbolic dynamics approach.* International Journal of Fatigue, 2007. **29**(6): p. 1100-1114.

72. Mukherjee, K., et al., *Symbolic analysis of sonar data for underwater target detection.* Oceanic Engineering, IEEE Journal of, 2011. **36**(2): p. 219-230.

73. Ray, A., *Symbolic dynamic analysis of complex systems for anomaly detection.* Signal Processing, 2004. **84**(7): p. 1115-1130.

74. Wu, T., et al., *Rainstorm monitoring based on symbolic dynamics and entropy.* Procedia Environmental Sciences, 2011. **10**: p. 1481-1488.

75. Brida, J.G., D.M. Gómez, and W.A. Risso, *Symbolic hierarchical analysis in currency markets: An application to contagion in currency crises.* Expert Systems with applications, 2009. **36**(4): p. 7721-7728.

76. Brida, J.G. and L.F. Punzo, *Symbolic time series analysis and dynamic regimes.* Structural Change and Economic Dynamics, 2003. **14**(2): p. 159-183.

77. Daw, C.S., C.E.A. Finney, and E.R. Tracy, *A review of symbolic analysis of experimental data.* Review of Scientific Instruments, 2003. **74**(2): p. 915-930.

78. Rao, C., et al., *Review and comparative evaluation of symbolic dynamic filtering for detection of anomaly patterns.* Signal, Image and Video Processing, 2009. **3**(2): p. 101-114.

79. Li, R., A. Mita, and J. Zhou, *Symbolization‐based differential evolution strategy for identification of structural parameters.* Structural Control and Health Monitoring, 2013. **20**(10): p. 1255-1270.

80. Khatkhate, A., et al., *Anomaly detection in flexible mechanical couplings via symbolic time series analysis.* Journal of Sound and Vibration, 2008. **311**(3): p. 608-622.

81. Chakraborty, S., et al. *Symbolic identification for anomaly detection in aircraft gas turbine engines*. IEEE.

82. Wang, D., et al., *Probabilistic damage identification based on correlation analysis using guided wave signals in aluminum plates.* Structural Health Monitoring, 2010. **9**(2): p. 133-144.